Investigation of Graphene Quantum Dot Endocytosis

by

Ugur Can Topkiran

Bachelor of Science, 2022
Izmir Institute of Technology
Izmir, Turkey

Submitted to the Graduate Faculty of the
College of Science and Engineering
Texas Christian University
in partial fulfillment of the requirements
for the degree of

Master of Science

November 2025

APPROVAL

INVESTIGATION OF GRAPHENE QUANTUM DOT ENDOCYTOSIS

by

Ugur Can Topkiran

Master of Science Thesis approved:

Major Professor: Dr. Anton V. Naumov

Dr. C. Magnus L. Rittby

Dr. Hana Dobrovolny

Dr. Giridhar Akkaraju

For The College of Science and Engineering

This page is intentionally left blank

ACKNOWLEDGEMENTS

I am deeply grateful to my advisor and mentor, Dr. Anton Naumov, for the freedom he gave me to do my best. Among my committee, I thank Dr. Magnus Rittby, who taught me the power of mathematics, and Dr. Hana Dobrovolny for her guidance. Teşekkürler to Dr. Giridhar Akkaraju for our many conversations; I am still waiting for our conversation on What Is Life?. I also thank the Physics & Astronomy faculty and especially Dr. Peter Frinchaboy for the much-needed second wind they gave me. I am thankful for my former labmate, Dr. Alina Valimukhametova, and my current labmates, Himish Paul, Diya Vashani, and Dr. Pramita Sharma. Thanks to my friends in Texas: Ali Gasimli, Ilke Lal Durmaz, and İbrahim Enes Bozkurt; and to Dr. Sanjana Chowdury Cohn and Jason Cohn. Thanks to the Freudyen Depresifler: Kutay Ozyurt, Deniz Molovali, Dr. Yusuf Karli, Selçuk Şentürk, and Hakan Yeler. Finally, to my mom, dad, sister, and to Kelly Fitzgerald (and our cats), whose late-night debates sparked many ideas, thank you.

Tiger got to hunt,

Bird got to fly;

Man got to sit and wonder, “Why, why, why?”

Tiger got to sleep,

Bird got to land;

Man got to Tell himself he understand.

-The Books of Bokonon-

Table of Contents

ACKNOWLEDGEMENTS ii
LIST OF FIGURES AND TABLES v
LIST OF ABBREVIATIONS vii
1. Introduction 1
1.1. Motivation 1
1.2. Questions to be answered 2
1.3. Significance and innovation 3
1.4. Background Study 4
1.4.1. Graphene quantum dots 4
1.4.2. Endocytosis 5
1.4.3. Chemical Endocytosis Inhibitors 10
2. Experimental Methods, Materials and Equipments 16
2.1. Synthesis of NGQDs and RGQDs 16
2.2. Structural Characterization 17
2.3. Optical Characterization 18
2.4. Cell Culture 19
2.5. Cell Viability Assay 19
2.6. Cell Uptake Experiments and Chemical Inhibitors 20
2.7. Confocal Fluorescence Microscopy and Image Processing 21
3. Results and discussion 23
What are the structural and surface characteristics of GQDs that influence cellular uptake? 23
3.1. Size, surface functional group and charge characterization 23
3.2. Optical properties 29
3.3. Cell Viable concentrations of NGQDs and RGQDs in cancerous and non-cancerous cell lines 31
What are the dominant endocytosis pathways for GQD internalization and do these mechanisms differ in cancerous and non-cancerous cell lines? 33
3.4. Internalization/excretion study of GQDs 33
How does surface charge and surface functional groups effect GQD endocytosis? 39
3.5. RGQD uptake in HeLa cells 39
4. Conclusion 43
4.1. Conclusion 43

4.2. Questions answered....45
References....49
VITA....1
Abstract....3

LIST OF FIGURES AND TABLES

Figure 1. Molecular structure representations of RGQDs and NGQDs.

Figure 2. Endocytosis pathways and charge-dependent uptake of GQDs. a) Schematic representations of endocytosis paths present in both HeLa and HEK-293 cell lines. These illustrations detail the mechanism, receptors, and their ligands, utilized for each endocytosis pathway. b) Depiction of potential mechanism of action of receptor-mediated endocytosis pathways (CME and FEME) displaying the effects of GQD charge. Negatively-charged RGQDs exhibit affinity toward CME, while amine groups of NGQDs are attracted to negatively-charged functional groups of FEME receptors. Dashed blue lines indicate the secondary preference of NGQDs for CME.

Figure 3. Schematic representation of the experimental workflow for endocytosis inhibition and GQD internalization studies. Inhibitors (Cytochalasin D, Genistein, Filipin, Amiloride, Chlorpromazine, and Sodium azide) were dissolved in DMSO and applied to cells, followed by a 30 min incubation at 37 °C with 5% CO_2. GQDs were then introduced and incubated for up to 24 h to allow cellular uptake. After incubation, the cells were washed, fixed on coverslips, and analyzed using visible-range fluorescence microscopy to track GQD internalization.

Figure 4. a) HRTEM images of NGQDs, d) RGQDs with insets displaying the interlayer spacings and FFT. b) TEM images of NGQDs, e) RGQDs revealing the size distributions. c) Nanoparticle size distribution histogram of NGQDs (blue), f) RGQDs (green); the mean and standard deviation of the distributions are indicated within the plots. g) FTIR spectra of NGQDs (blue), h) RGQDs (green); the peaks are marked with the corresponding functional groups present within the structure.

Figure 5. AFM height profiles for a) NGQDs and b) RGQDs.
Figure 6. (a) XPS survey spectrum of RGQDs (b) Deconvoluted C1s XPS spectra of RGQDs from Voigt fit with Shirley background correction (c) Deconvoluted O1s XPS spectra of RGQDs from Voigt fit with Shirley background correction.

Figure 7. (a) XPS survey spectrum of NGQDs (b) Deconvoluted N1s XPS spectra of RGQDs from Voigt fit with Shirley background correction (c) Deconvoluted C1s XPS spectra of RGQDs from Voigt fit with Shirley background correction (d) Deconvoluted O1s XPS spectra of RGQDs from Voigt fit with Shirley background correction.

Figure 8. ζ-potentials of NGQDs (blue) and RGQDs (green) at pH 7.

Figure 9. a) Absorbance spectra of NGQDs (blue) and RGQDs (green). b) Visible fluorescence spectra of NGQDs and RGQDs under 400 nm laser excitation.
Figure 10. a) Cell viability NGQDs (blue) in HeLa and b) HEK-293 cells. c) Cell viability of RGQDs (green) in HeLa and d) HEK-293 cells as evaluated via MTT assay.

Figure 11. Emission spectra of a) genistein (red), b) filipin (yellow) and c) chlorpromazine (blue) measured at 460 nm excitation at the concentrations used for the experiment. Spectra displays that these three inhibitors do not contribute to the fluorescence under 460 nm excitation.

Figure 12. a) Normalized corrected total cell fluorescence (CTCF (%)) of NGQDs in Hela and HEK-293 cells in the presence of chemical inhibitors at 6, 12, and 24 h. b) Bright-field/VIS fluorescence confocal overlay images of HeLa cells treated with NGQDs in the presence of chemical inhibitors at 12 h time point. Scale bar = 10 μm.

Figure 13. Bright-field/VIS fluorescence confocal overlay images of HeLa cells at 6 and 24h, HEK293 cells at 6 and 12h treated with NGQDs in the presence of chemical inhibitors. Scale bar = 10 μm.

Figure 14. Comparative internalizations of NGQDs and RGQDs in HeLa cells with DMSO treatment (control group) at 6, 12 and 24 h. Corrected total cell fluorescence (CTCF (%)) was normalized to the highest fluorescence value observed (NGQD at 6h) to assess the comparative internalizations of NGQDs and RGQDs when no inhibitors are present.

Figure 15. a) Normalized corrected total cell fluorescence (CTCF (%)) of RGQDs in Hela in the presence of chemical inhibitors at 6, 12 and 24 h. b) Bright-field/VIS fluorescence confocal overlay images of HeLa cells treated with RGQDs in the presence of chemical inhibitors at 6, 12 and 24 h. Scale bar = 10 μm.

Figure 16. Normalized corrected total cell fluorescence (CTCF (%)) of NGQDs (blue) compared to RGQDs (green) in Hela cells at 6 h.

Table 1. Internalization paths present in HeLa and HEK-293 cell lines. (✓) present, (✕) the lack of key molecular component, (○) conflicting evidence.

Table 2. List of chemical endocytosis inhibitors used in the experiment, their mechanisms of action, and their target pathways. (✓) - proposed target pathway, (●) off- target pathways of inhibitors.

LIST OF ABBREVIATIONS

AFM: Atomic force microscopy

ATR: Attenuated total reflectance

Cav: Caveolin-mediated endocytosis

CLIC/GEEC: Clathrin-independent carriers / GPI-anchored protein-enriched early endosomal compartments

CME: Clathrin-mediated endocytosis

CMOS: Complementary metal–oxide–semiconductor

CTCF: Corrected total cell fluorescence

DMSO: Dimethyl sulfoxide

DSU: Disk spinning unit (confocal)

EGFR: Epidermal growth factor receptor

FEME: Fast endophilin-mediated endocytosis

FFT: Fast Fourier transform

FTIR: Fourier transform infrared

GO: Graphene oxide

GPCRs: Guanine nucleotide-binding protein-coupled receptors

GQDs: Graphene quantum dots

HEK-293: Human embryonic kidney 293 (cells)

HRTEM: High-resolution transmission electron microscopy

HUVEC: Human umbilical vein endothelial cells

IGF1R: Insulin-like growth factor 1 receptor

MEM: Minimum essential medium

LIST OF ABBREVIATIONS

MTT: 3-(4,5-dimethylthiazol-2-yl)-2,5-diphenyltetrazolium bromide

NaN3: Sodium azide

NGF R: Nerve growth factor receptor (NGFR)

NGQDs: Nitrogen-doped graphene quantum dots

NIR: Near-infrared

PBS: Phosphate-buffered saline

PDGFR: Platelet-derived growth factor receptor

Phago: Phagocytosis

PM: Plasma membrane

RGQDs: Reduced graphene oxide derived graphene quantum dots

ROI: Region of interest

RTKs: Receptor tyrosine kinases

SWCNTs: Single walled carbon nanotubes

TEM: Transmission electron microscopy

UV: Ultraviolet

UV–Vis–NIR: Ultraviolet–visible–near-infrared

VEGFR: Vascular endothelial growth factor receptor

VIS: Visible

XPS: X-ray photoelectron spectroscopy

1. Introduction

1.1. Motivation

Due to their remarkable properties, graphene quantum dot (GQD) research has grown rapidly over the past decade. A recent Web of Science analysis, covering publications related to GQDs, identified approximately 24,600 papers published between 2004 and early 2024, with a pronounced surge beginning around 2014 [1][2]. Graphene quantum dots (GQDs) are zero-dimensional sp^2-carbon nanostructures (<20 nm) with high water solubility and surface chemistry [3, 4]. They can be produced by top-down oxidation/exfoliation of graphene derivatives or bottom-up hydrothermal carbonization of small precursors [4, 5]. Their surface functional groups enable π–π stacking, electrostatic interaction, and covalent conjugation with therapeutic/targeting cargo (e.g., biomolecules, plasmid DNA, siRNA, CRISPR-Cas9 RNPs) [6-9]. Moreover, GQDs exhibit substantially photostable fluorescence in the visible (Vis) and near-infrared NIR ranges upon 808 nm excitation, enabling tissue penetrating, non invasive bio-imaging and -sensing [2, 10, 11]. Endocytosis supports nutrient uptake, membrane homeostasis, synaptic signaling, and immune responses through multiple distinct pathways [12]. Due to their nanoscale size, nanomaterials are expected to go through cell uptake through endocytosis. Poor targeting of these routes can activate cellular defenses, including MPS-mediated clearance of non-internalized nanomaterials [13]. Thus, a thorough understanding of nanoparticle entry mechanisms can help prevent triggering undesirable processes that might hamper the transition of GQD-based nanomedicines to the clinic. The present work aims to fill

the gap in the literature by introducing a holistic approach to the assessment of potential GQD entry pathways [14].

1.2. Questions to be answered

i. **What are the structural and surface characteristics of GQDs that influence cellular uptake?**

Here, prior to identifying the endocytosis pathways responsible for GQD internalization, we will characterize the GQD morphology, surface charge, and optical properties. Transmission electron microscopy (TEM), atomic force microscopy (AFM), Fourier transform infrared spectroscopy (FTIR), and X-ray photoelectron spectroscopy (XPS) will be employed to determine morphology and surface functional groups, while ζ-potential measurements will be used to evaluate surface charge. The concentrations suitable for cell studies will be established through cell viability assays. This work will be presented in Chapters 3.1–3.3.

ii. **What are the dominant endocytosis pathways for GQD internalization and, do these mechanisms differ in cancerous and non-cancerous cell lines?**

Herein, a holistic approach to cell uptake studies by utilizing six different inhibitors while considering their on- and off-target effects on internalization of the GQDs of different charges is provided. Internalization is assessed *in vitro* through corrected total cell fluorescence (CTCF) analysis. As a way to evaluate endocytosis pathway differences between non-cancer and cancer cells, GQD internalization is studied in this work in model

cancer (HeLa) and non-cancer (HEK-293) cell lines. Based on the inhibition effects observed, we will identify the dominant pathways responsible for uptake in each cell line and assess differences between cancerous and non-cancerous models. This study will be covered in Chapter 3.4.

iii. How do surface charge and surface functional groups influence GQD endocytosis?

At this stage, we will study how GQD surface chemistry guides uptake by comparing positively charged, nitrogen-doped graphene quantum dots (NGQDs), with negatively charged, Reduced graphene oxide derived graphene quantum dots (RGQDs), in HeLa cells. Using an aforementioned six-inhibitor panel, we will attribute pathway preferences through analyzing their internalization by confocal fluorescence microscopy. We will identify the influence of charges and functional-groups on uptake mechanisms of GQDs and will present and discuss the results in Chapter 3.5.

1.3. Significance and innovation

The **significance** of this work is in establishing a mechanistic basis of GQD endocytosis that takes the plasma membrane (PM) structure into account. By resolving the inconsistencies in the literature, this work will enable case-specific nanomaterial design, increasing the efficiency of targeted delivery applications and paving the way to future clinical applications for GQDs. In this work, we provide an **innovative**, holistic framework that instead of studying one or few entry pathways separately, evaluates multiple endocytic routes with a multi-inhibitor approach while rigorously analyzing their on- and off-target effects. Furthermore, we

provide a novel surface functional group- and charge-dependent description of uptake pathway preferences for GQDs in cancerous and non-cancerous cell lines. The objectives will be accomplished by: (1) definitive morphology, surface, and optical characterization of NGQDs and RGQDs; (2) comprehensive mapping of endocytosis path inhibitors and their on-/off-target effects (3) uptake analysis by confocal fluorescence microscopy; (4) direct comparison of uptake pathways between cancerous and non-cancerous cell lines; (5) establishing the relationship between GQD surface charge, functional groups, and pathway selectivity during endocytosis by comparing internalization of positively charged NGQDs and negatively charged RGQDs.

1.4. Background Study

1.4.1. Graphene quantum dots

As noted in Section 1.1, interest in the biomedical applications of GQDs has surged over the last decade [2]. GQDs show outstanding biocompatibility among nanocarbons, demonstrated both *in vitro* and *in vivo*. Conjugation modes (π–π stacking on the graphitic surface (Figure 1), electrostatic attraction toward surface functional groups, and covalent attachment) enable loading of therapeutics and attachment targeting ligands. GQDs possess visible fluorescence arising from size-dependent quantum confinement [10], and several structures have recently been engineered to exhibit fluorescence in the NIR originating from defect states at multiple functional groups [5, 15]. Their optical properties have paved the way for GQD-based sensors for detecting proteins [16], RNA [17], micro RNA [18], single-stranded DNA [19], and small molecules [2]. GQDs can be synthesized at scale and low cost

for high-throughput drug screening, and they display rapid cellular uptake with fast clearance from cells and organs, unlike many other nanomaterials residing in biological tissues for prolonged periods [3]. In this thesis, NGQDs and RGQDs are used to examine how surface charge and functional groups influence endocytic uptake.

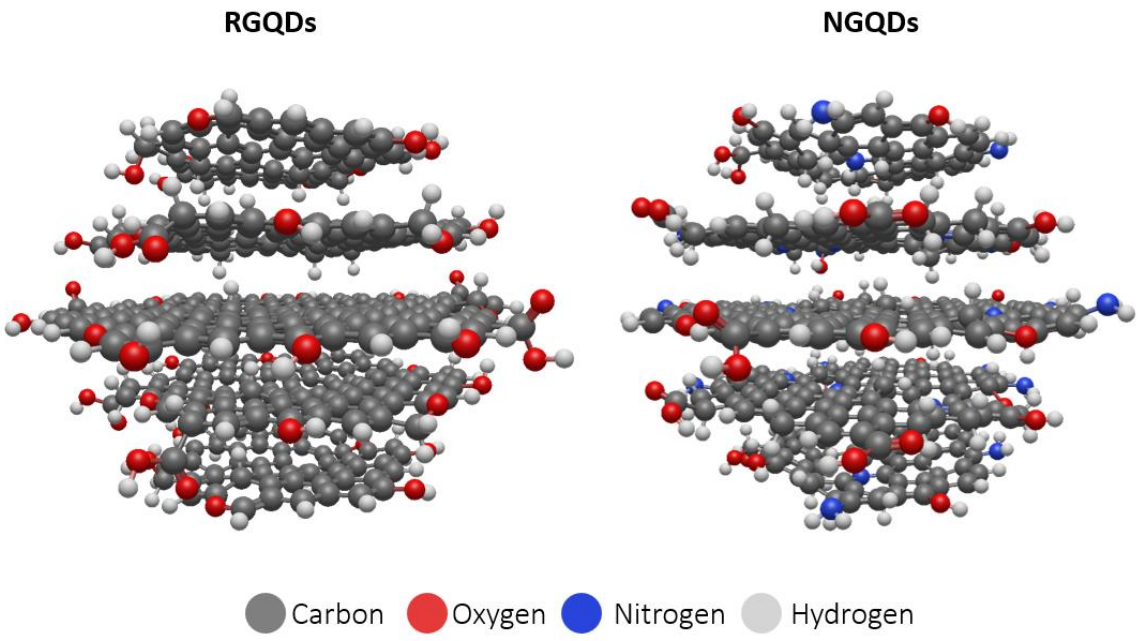

Figure 1. Molecular structure representations of RGQDs and NGQDs.

1.4.2. Endocytosis

Due to their small size, GQDs (3–15 nm) are expected to be internalized predominantly by endocytosis [20, 21]. Even though GQDs are used in multiple therapeutic applications, their cellular uptake is not sufficiently studied through receptor-mediated endocytosis or cell membrane diffusion. Receptor coated pits only occupy around 2-3 % of the cell membrane, however, they internalize an area comparable to the entire membrane roughly every two hours [22, 23]. This high turnover enables efficient uptake of larger cargos such as nanomaterials, making endocytosis a primary route despite low receptor surface occupancy. Conversely, failure to target the appropriate pathways can trigger cellular defenses, including clearance of non-internalized nanomaterials by the mononuclear phagocytic system (MPS) [13]. Thus, a thorough understanding of nanoparticle entry mechanisms is essential to avoid such undesirable responses, hampering the transition of nanomedicines to the clinic.

Endocytosis begins when a nanoparticle engages the plasma membrane, and the selection of the pathway is dependent on the functional groups present on the surface, the charge, the size, and the shape of the nanoparticle. For example, sheet-like materials such as graphene oxide (GO) follow different pathways as lateral size changes: smaller flakes are typically routed through clathrin-mediated endocytosis (CME), whereas larger ones are reported to enter via phagocytosis (Phago) [24]. In addition to these, several other mechanisms can facilitate nanomaterial uptake. CME, a dynamin-dependent uptake, forms ~100 nm vesicles, setting the upper size limit for cargo internalized by this route [25]. Fast endophilin-mediated endocytosis (FEME) is another dynamin-dependent but clathrin-independent path. It facilitates extremely rapid entry (<10s) through 60–80 nm tubular carriers that can extend several hundred nanometers on the cell membrane, enabling nanomaterial trafficking [26]. In contrast, clathrin-independent/dynamin-independent endocytosis is mediated by clathrin-independent vesicles

arising from the plasma membrane and maturing into tubular endocytic compartments named Clathrin-independent carriers / GPI-anchored protein-enriched early endosomal compartments (CLIC/GEEC) [27]. Sharing similarities with FEME through their localization to the edge of migrating cells and involvement of ring-shaped tubular pleomorphic vesicles, it is observed to be a distinct high-capacity pathway in mammalian cultured cells. In clathrin independent uptake, the extracellular mechanism is operated through galectin-3 lectin proteins, triggering the formation of the CLIC/GEEC vesicles [28]. Contrary to FEME, CLIC/GEEC shows continuous uptake without the need for a receptor trigger stimulated through specific ligand-receptor interactions [29].

Caveolin-mediated endocytosis is distinguished by a ~60 nm bulb-shaped pit connected to the plasma membrane by a narrower neck and generally accommodates smaller particles (sizes ~50 nm or less) [30]. Employed in the uptake of particles with a size larger than 200 nm, Macropinocytosis (Macro) and Phago are two of the most studied dynamin-independent but actin-dependent pathways. Even though the formation of the phagocytosis vesicles is triggered by scavenger receptors, GQD sizes are below the Phago uptake limit, which makes scavenger receptor-mediated GQD endocytosis unlikely [31]. Several other endocytosis pathways are lipid raft-dependent where lipid raft's complex structure can allow the uptake of the same cargo through multiple endocytosis pathways [32]. Dynamin present in both CME and FEME is shown to be an indicator of lipid raft-dependency of an endocytosis pathway [33]. However, Cav, a dynamin- and clathrin-independent, is also reported to be a possible lipid raft-dependent pathway [34]. For another carbon nanomaterial, single walled carbon nanotubes (SWCNTs), internalization is predominantly carried through energy-dependent endocytosis (CME, Cav, and Macro depending on the tube length) where SWCNT association with lipids alters the

membrane tension, therefore stimulating endocytosis on the membrane [35]. Endocytosis is observed to be the main internalization route for SWCNTs since they lack sufficient insertion energy to penetrate the plasma membrane of a cell via a membrane-piercing process of nanospearing [36].

Although membrane diffusion has been shown to be the predominant uptake mode for single-layer GQDs in the ~2-7 nm range [37], the evidence displaying membrane diffusion uptake of multi-layer GQDs is lacking. Prior endocytosis work on carbon-based nanomaterials performed with larger graphene oxide or carbon oxide particles of sizes ranging from 100 to 300 nm displays cellular uptake through a combination of CME and Cav, suggesting multiple pathway mechanisms for larger structures [38-41]. Moreover, GO flakes of ~ 200 to 300 nm sizes are reported to use CME whereas smaller flakes of sizes ~100 nm internalize through Cav [42]. GQDs being still substantially on a smaller end of the scale and displaying a plethora of surface functional group combinations, present a different platform to nanomaterial endocytosis through PM interactions. Due to a scarcity of GQD-specific studies, its cellular internalization mechanisms are often mistakenly associated with the uptake of other carbon nanomaterials. Studying the GQDs' endocytosis process will deepen insights into nanoparticle/cell membrane interactions that will assist in avoiding cell defense mechanisms, and increasing internalization efficiency. Since different cell types use different endocytosis pathways, understanding how GQDs are taken up can also help target specific cells and improve drug delivery efficiency.

Previously, Wang et al. reported that hollow carbon dots made from bovine serum albumin and used to deliver doxorubicin, enter A549 cells via vesicle formation that later fuses with lysosomes, attributing uptake to endocytosis [43]. Work in human neural stem cells showed

that GQD uptake is dependent on both exposure time and dose concentration-dependent manner [44]. Following studies proposed that GQDs primarily use Cav in MCF-7 and MGC-803 cells [45], and CME in HUVEC and cells HeLa [46] as well as in *Trypanosoma brucei* [47]. These conclusions were based on the substantial decrease of intracellular GQD fluorescence upon cell treatment with corresponding chemical pathway inhibitors. GQD endocytosis studies by Xu et al. consider a possible combination of CME and Cav pathways [48]. Thus the need for a holistic approach that recognizes the possibility of multiple concurrent routes for nanomaterial entry is essential for GQDs as has been emphasized for other nanomaterials [49, 50]. Different and often conflicting conclusions in the current literature may arise from testing only a few chemical endocytosis inhibitors and overlooking their off-target effects. This can result in assigning sub-10 nm GQD entry to Macro or Phago [51, 52] pathways, even though these mechanisms typically favor much larger cargos (~200 nm to 0.5 μm). In addition, the roles of GQD surface charge, different functional groups, and receptor-ligand interactions within the endocytotic cell membrane structures need to be accounted for.

Cell line	**Internalization paths**				
	CME	FEME	Cav	CLIC/GEEC	Macro
HeLa	✓	✓[53]	✓[54]	✕[55, 56]	✓
HEK-293	✓	✓[57]	✕[58]	○[59]	✓

Table 1. Internalization paths present in HeLa and HEK-293 cell lines. (✓) present, (✕) the lack of key molecular component, (○) conflicting evidence.

Prior to providing the background on chemical endocytosis inhibitors used in this study, the internalization pathways of each cell line need to be discussed. Both HeLa and HEK-293 cells allow for internalization through CME, FEME, and Macro, whereas only HeLa cells

possess the Cav pathway [54] (Table 1). Uptake through lectin-dependent endocytosis, CLIC/GEEC, is not found in the HeLa cell line, while some conflicting results are reported about its presence within HEK-293 cells [55, 56, 59].

1.4.3. Chemical Endocytosis Inhibitors

In this chapter, we aim to provide a comprehensive background for understanding the potential GQD entry pathways using six common chemical endocytosis inhibitors [24, 46, 47, 51], each with a different mechanism of action.

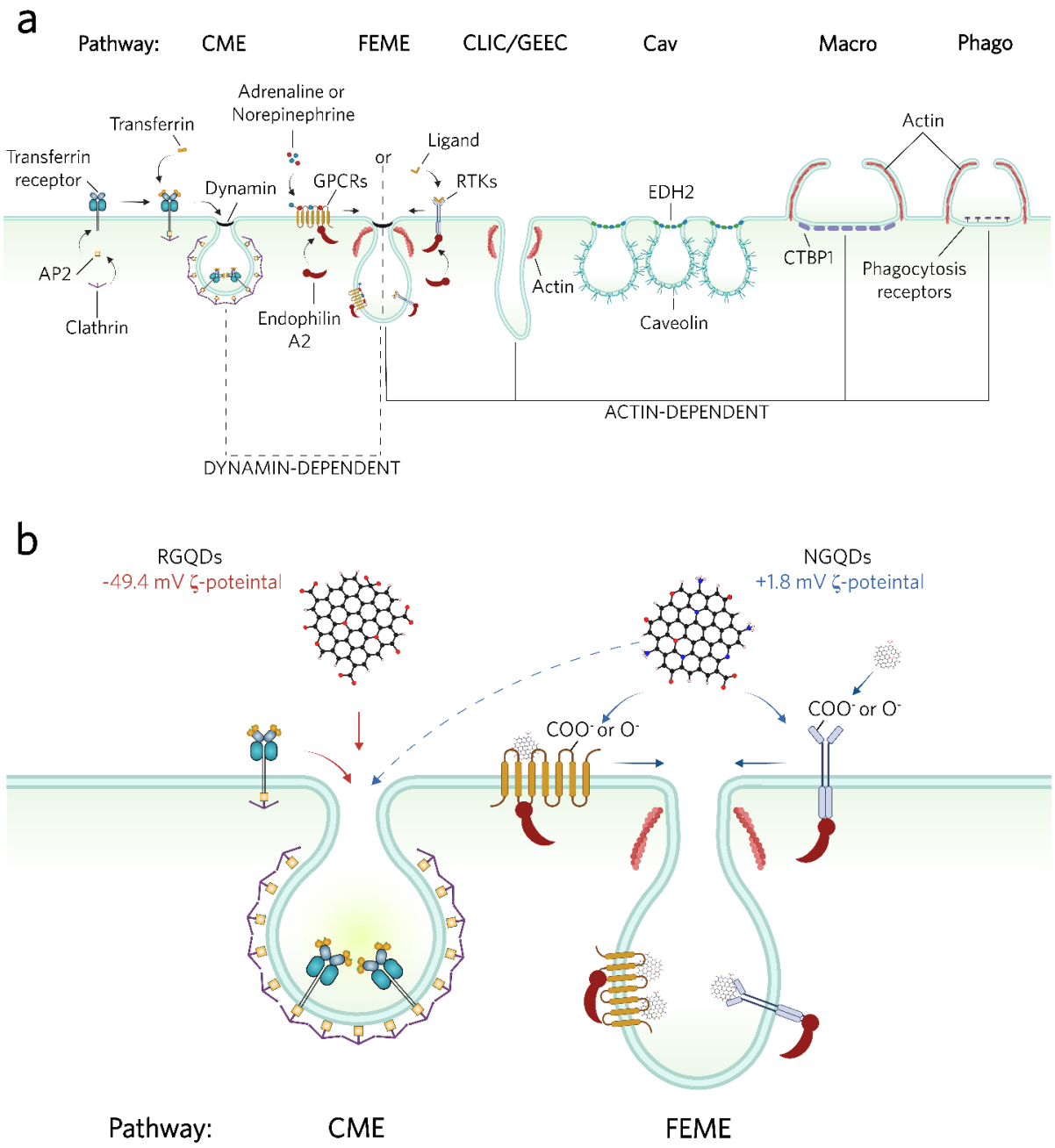

Figure 2. Endocytosis pathways and charge-dependent uptake of GQDs. a) Schematic representations of endocytosis paths present in both HeLa and HEK-293 cell lines. These illustrations detail the mechanism, receptors, and their ligands, used for each endocytosis pathway. b) Depiction of potential mechanism of action of receptor-mediated endocytosis pathways (CME and FEME) displaying the effects of GQD charge. Negatively-charged

RGQDs exhibit affinity toward CME, while amine groups of NGQDs are attracted to negatively-charged functional groups of FEME receptors. Dashed blue lines indicate the secondary preference of NGQDs for CME.

The first inhibitor studied in the present work, **cytochalasin D**, is commercially marketed as a Macro and Phago target inhibitor (Table 2). The primary mechanism of action for cytochalasin D involves depolymerization of F-actins, a process that not only impacts its intended targets but also plays a role in disrupting other pathways employing actins (Figure 2a) [60, 61]. Given its broad influence, inhibition data obtained with cytochalasin D must be interpreted cautiously when evaluating GQD internalization. Since GQDs are smaller than the usual size threshold required to trigger Macro (Figure 1c,f), attributing any observed reduction in uptake in cytochalasin D treated cells solely to that pathway may be misleading. A more likely explanation is that GQDs employ a combination of internalization routes such as FEME and CLIC/GEEC, both sensitive to actin depolymerization[26, 27], alongside to CME and Cav, since actin filaments contribute to vesicle formation in FEME and CLIC/GEEC [61].

Inhibitors	Mechanism of action	Endocytosis Pathways						Evaluations
		CME	FEME	Cav	CLIC/ GEEC	Macro	Phago	
Cytochalasin D	F- actin depolymeri-zation[60]	●	●	●	●	✓	✓	F-Actin depolymerization affects most paths[61]
Genistein	Tyrosine kinase inhibitor[62]	●	●	●	●	●	●	Partially inhibits Cav[63] Could inhibit other receptor-mediated endocytosis[64] and Macro[65]
Filipin	Binds to membrane cholesterol and disassociates actin-binding proteins[66]	●	✓					Inhibits CME but toxic at high concentrations[67]
Amiloride	Na ion channel, Na/H ion exchange inhibition and possibly induces the disassembly of actin stress fibers[68, 69]		●			✓		Revealed to inhibit FEME[26, 69]
Chlorproma-zine	Inhibits the binding of AP2 and clathrin[70]	✓	●	●				Inhibits off-target FEME[26]
Sodium azide	Inhibits glycolysis and ATP production in cells[71, 72]	✓	✓	✓	✓	✓	✓	Inhibits all energy-dependent paths

Table 2. List of chemical endocytosis inhibitors used in the experiment, their mechanisms of action, and their target pathways. (✓) - proposed target pathway, (●) off- target pathways of inhibitors.

Further literature analysis unveils the challenges of using **genistein**, a broad-spectrum tyrosine-specific protein kinase inhibitor [62]. While kinase inhibition is shown to partially suppress Cav, it can affect other pathways involving protein kinases. They participate throughout receptor-mediated endocytosis, from regulating vesicle formation to controlling receptor recycling [63, 64]. For example, although Macro is not known to be a receptor-mediated pathway, it can also be inhibited by genistein, since the formation of Macro is regulated by growth factor signaling, and growth factors activate their respective receptor tyrosine kinases (RTKs). Therefore, the disruption of tyrosine kinase also inhibits the endocytosis vesicle formation for that process [65].

Filipin, similar to genistein, interacts with the membrane cholesterol where its mechanism of action is carried through the disruption of actin-binding proteins [66, 67], suggesting possible off-target inhibiton for actin-dependent FEME and CLIC/GEEC pathways (Figure 2a). Filipin is also observed to strongly inhibit the formation of the endophilin assemblies essential to FEME [26], while at high concentrations, filipin can lead to off-target inhibition of CME [67].

Amiloride is considered relatively specific, targeting Na^+ channels to inhibit Na^+/H^+ exchange. Nevertheless, amiloride is a micropinocytosis inhibitor, where its mechanism of action may induce the disassembly of actin stress fibers. This process likely drives the reorganization of the actin cytoskeleton, which, in turn, is shown to influence FEME dynamics [26, 68, 69].

Chlorpromazine is a cationic amphiphilic drug that inhibits receptor recycling. This mechanism of chlorpromazine halts the congregation of adaptor proteins (AP2) and clathrin on endosomal membranes, thereby suppressing the formation of clathrin-coated pits on the plasma membrane. The important role of AP2 in the construction of the endocytic pit implies that its relocation could perturb a clathrin-mediated pathway (Figure 1a) [70, 73]. Chlorpromazine also displays non-target FEME inhibition by endophilin-positive assembly disruption [26].

The sixth inhibitor, **sodium azide** is renowned for its mechanism of action that interferes with the mitochondrial electron transport chain, causing a rapid intercellular ATP depletion [74] and mitochondrial flavoprotein NADH dehydrogenase inhibition [75]. Glycolysis inhibition provided by sodium azide allows the study of passive and/or facilitated diffusion of GQDs into the cells. Unlike endocytosis, which is highly energy dependent, both passive and/or facilitated diffusion do not require ATP [22]. Therefore, the lack of inhibition upon sodium azide treatment is expected to indicate that GQDs utilize passive and or facilitated diffusion. However, it is important to note that sodium azide broadly inhibits all energy-dependent pathways, complicating the study of nanomaterial endocytosis due to its lack of selectivity [72]. This examination, therefore, highlights the intricate interplay among different endocytosis pathways and emphasizes the importance of multifaceted analysis in inhibitor-based studies.

2. Experimental Methods, Materials and Equipments

2.1. Synthesis of NGQDs and RGQDs

To synthesize RGQDs, High porosity RGO (HP-RGO-025G, Graphene Supermarket, Ronkonkoma, NY, USA) was oxidized. The reaction was carried out as follows: RGO was dispersed in deionized (DI) water at 0.25 mg/mL concentration and 1 mL of sodium hypochlorite (LC246364, LabChem, Zelienople, PA, USA) was added to the suspension. Upon the introduction of NaOCl into aqueous RGO, its decomposition led to the formation of highly reactive oxygen free radicals reacting with RGO graphitic structure, yielding nano-sized RGQDs. The vials were gently shaken, capped, and left to react for two days in a dark environment under ambient conditions. Products were further purified from unreacted NaOCl and small organic fragments via dialysis in a 1 kDa molecular cutoff dialysis bag (132104, Repligen, Waltham, MA, USA) against DI water for 24 h. For the first 3 hours, water in the dialysis chamber was changed every 30 minutes, after that – every 7 hours. After dialysis, the purified suspension was processed through a 0.22 μm syringe filter to remove the unreacted RGO and sterilize the product.

To synthesize NGQDs with a bottom-up approach, 4 g glucosamine hydrochloride (Sigma-Aldrich batch #104K0082) was dispersed in 250 mL of DI water and the mixture was microwave-treated in an HB-P90D23AP-ST Hamilton Beach microwave oven for 60 min at 1350 W power. During the microwave treatment, glucosamine underwent a dehydration reaction, leading to its polymerization and formation of NGQDs. After the synthesis, the product was purified from molecular precursors using a 1kDa dialysis bag (132104, Repligen, Waltham, MA, USA) in DI water for 24 h. For the first 3 hours, water in the dialysis chamber

was changed every 30 minutes, after that – every 7 hours. Both products were further air-dried to adjust the concentration to 10.5 mg/mL for RGQDs and to 21.0 mg/mL for NGQDs.

2.2. Structural Characterization

The assessment of the nanoscale graphitic structure of the GQDs was performed via HRTEM (high-resolution transmission electron microscopy, JEOL JEM-2100). For TEM analysis, GQDs were diluted in DI water (1–3 mg/mL), bath-sonicated to prevent aggregation, and drop-cast (3 μL) onto a 400-mesh holey carbon film and will be left drying under ambient conditions. The average size of the GQD structures was derived from TEM analysis, while HRTEM is used to ensure their graphitic structure. Size distributions were obtained by imaging approximately 100 particles per sample, followed by histogram analysis. HRTEM was also used to visualize lattice fringes and calculate interlayer spacing based on diffraction contrast patterns. As the electron beam travels through the sample, the crystal lattice acts as a diffraction grating forming interference patterns. These interference patterns allow us to obtain interlayer spacings of GQDs.

Infrared absorption was evaluated via the attenuated total reflection (ATR) mode of a Thermo Nicolet Nexus 670 FTIR to identify functional groups present on the GQD surface. Samples for FTIR measurements were freeze-dried using a Labconco FreeZone 4.5 freeze dryer.

A comprehensive surface analysis was performed using FTIR and XPS. Samples initially were freeze dried and used in powder form for both methods. In FTIR spectroscopy, frequency of the absorbed light coincides with specific molecular bond vibrations giving molecular vibration fingerprints of surface functional groups. Attenuated Total Reflectance

(ATR) mode used for FTIR spectroscopy uses a crystal (of higher refractive index than the sample) to facilitate a total internal reflectance. Powder GQDs are placed on top of the crystal and only the evanescent wave penetrates and interacts with only a few microns of the sample, providing the vibrational spectra that displays the surface functional groups of GQDs.

In addition to FTIR analysis, surface functional groups of both GQDs were characterized with Kratos Analytical Axis Supra+ X-ray photoelectron spectrometer. Samples were pelletized at 10,000 psi for 30s to form 3mm x 3mm x 1mm pellets for mounting in the XPS instrument and spectra were taken using the Al Kα x-ray source operating at 220.00 W with an emission current of 15.00 mA. Bruker MultiMode 8 Atomic Force Microscope in tapping mode was used to obtain the height profiles of both GQDs.

XPS uses the photoelectric effect as the sample is irradiated with x-rays and the kinetic energy of the emitted electrons is analyzed. The kinetic energy of these emitted electrons is measured to determine their binding energy, providing elemental composition and information on the surface functional groups of the GQDs.

2.3. Optical Characterization

The UV-Vis-NIR absorbance of GQD samples was acquired within the 200-1000 nm range using an Agilent Technologies (Cary 60) absorption spectrometer while their photoluminescence spectra were recorded with Horiba SPEX NanoLog fluorescence spectrofluorometer. ζ Potentials of different GQD suspensions at 1 mg/mL were measured using a NanoBrook ZetaPALS instrument to reflect their surface charge.

2.4. Cell Culture

In vitro studies were performed using human embryonic kidney (HEK-293) cells as the model non-cancer cell line and HeLa cells as the model cancer cell line. The cells were cultured in Dulbecco modified Eagle's medium (D6046, Sigma-Aldrich) and 10% fetal bovine serum (16140-063, Gibco) with the addition of 1% L-glutamine (G7513, Sigma-Aldrich), the minimum essential medium (MEM), nonessential amino acid solution (M7145, Sigma-Aldrich) and penicillin/streptomycin (P4333, Sigma-Aldrich). Cell cultures were kept in an incubator with 5% CO2 at 37 °C and used for cell viability assays, cell uptake experiments, and fluorescence microscopy experiments.

2.5. Cell Viability Assay

Standard MTT cell viability assays were employed to assess the biocompatibility of the GQDs. Both HeLa and HEK-293 cells were plated in a 96-well plate at a density of 5000 cells per well (100 μL well-1) and kept in an incubator overnight at 37.1 °C with 5% CO2. After 24 h incubation, the medium was replaced by 100 μL of 1 mg/mL of thiazolyl blue tetrazolium bromide. After 4 h of further incubation, 3-(4-dimethylthiazol-2-yl)-2,5-diphenyltetrazolium bromide (MTT) was replaced with 100 μL of DMSO (dimethyl sulfoxide) to solubilize the formazan, a highly absorbing, blue-colored byproduct formed in metabolically active cells. The absorbance of formazan, proportional to cell viability, was measured in each well at 580 nm using a FLUOstar Omega microplate reader.

2.6. Cell Uptake Experiments and Chemical Inhibitors

Both HeLa and HEK-293 cells were seeded at 1×10^4 cells onto glass coverslips placed in a six-well plate with 2 mL media in each well and incubated for 24 h at 37.1 °C with 5% CO2. Cells were treated with 100 µL each: DMSO (0.5%) for control samples, or 532 µg/mL Amiloride hydrochloride hydrate, or 142 µg/mL Chlorpromazine hydrochloride, or 40 µg/mL filipin complex from Streptomyces filipinensis, or 100 µg/mL cytochalasin D, or 1.081 mg/mL genistein, or 3.901 mg/mL sodium azide (NaN3) for samples subjected to different endocytosis inhibitors. All inhibitors were bought from Sigma-Aldrich (USA) in powder form and dissolved in DMSO. Treated cells were left in an incubator for 30 minutes, sufficient for endocytosis pathway inhibition to take place. Afterward, 100 µL of 21 mg/mL NGQDs or 10.5 mg/mL of RGQDs were added to the cells and left to internalize for 6 h, 12 h, and 24 h. Coverslips with cells were further washed with 1× phosphate-buffered saline (PBS) to remove GQDs that did not internalize. Following the washing step, the cells were fixed with 4% formaldehyde solution (28908, Thermo Scientific) and 1×Fluoromount-GTM mounting medium (00-4958-02, Invitrogen) and sealed onto microscope slides for imaging (Figure 3).

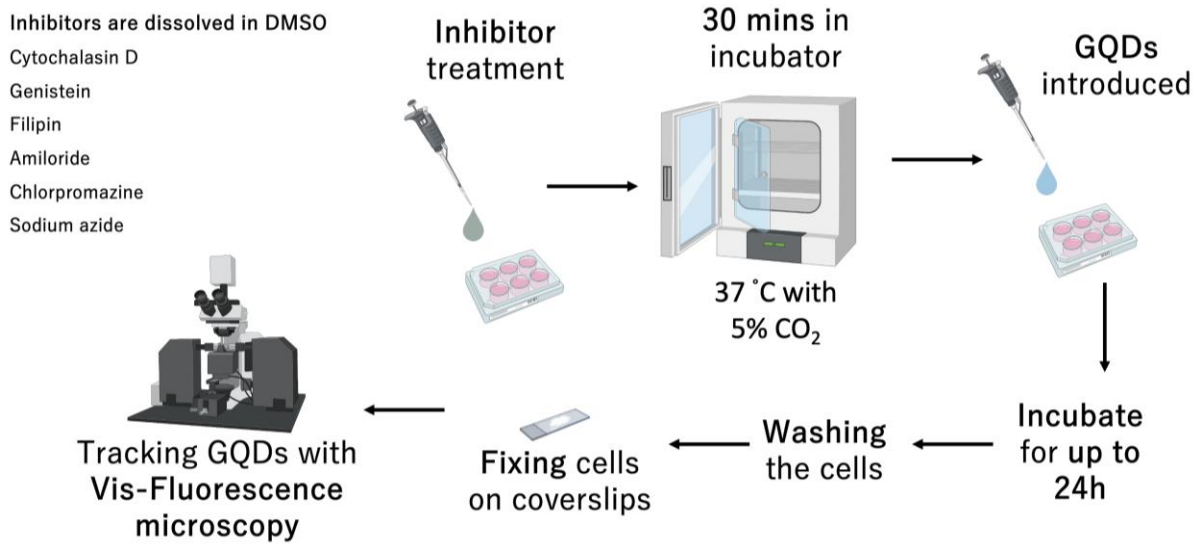

Figure 3. Schematic representation of the experimental workflow for endocytosis inhibition and GQD internalization studies. Inhibitors (Cytochalasin D, Genistein, Filipin, Amiloride, Chlorpromazine, and Sodium azide) were dissolved in DMSO and applied to cells, followed by a 30 min incubation at 37 °C with 5% CO_2. GQDs were then introduced and incubated for up to 24 h to allow cellular uptake. After incubation, the cells were washed, fixed on coverslips, and analyzed using visible-range fluorescence microscopy to track GQD internalization.

2.7. Confocal Fluorescence Microscopy and Image Processing

Fluorescence microscopy imaging in the visible was done with a semi-motorized inverted Olympus IX73 fluorescence microscope with a 60× (IR-corrected Olympus Plan Apo) water immersion objective coupled to a Photometrics Prime 95B CMOS camera through an Olympus DSU (disk spinning unit) confocal system. Images were taken with 480 ± 20 nm filtered lamp excitation and 535 ± 20 nm emission filter for both GQD types.

Image J software (1.53a, National Institutes of Health, Bethesda, MD, USA) was used for the assessment of the intercellular fluorescence intensity. Corrected total cell fluorescence (CTCF) was calculated to quantify cellular internalization. CTCF is calculated by subtracting the product of the area of the selected cell and the mean fluorescence of background readings from the integrated density of the cell:

$$CTCF = Normalized\ Integrated\ Density - (Area\ of\ selected\ cell \times \text{The mean fluorescence of background readings})$$

Normalized Integrated Density is defined as the mean value of the pixel brightness in the selected cell multiplied by the total area of the cell. The mean fluorescence of the background reading is represented as the normalized integrated density of the background per unit area.

Initially regions of interest (ROI) were obtained by outlining each individual cell (~ 100 cells per treatment at one time point for each cell line and nanomaterial. In total >4000 cells for NGQDs and >2000 cells for RGQDs are outlined and analyzed). Intracellular fluorescence is reflected in the Integrated Density, the mean gray value for each pixel within the selected ROI. Later, to account for background fluorescence signal, Integrated Density of an empty area the size of a cell is subtracted from the Integrated Density of each cell. In order to inter-compare the results, all fluorescence data within Figure 5 and Figure S7 is normalized to the corresponding highest internalization time point, 6 h for NGQDs and 12 h for RGQDs respectively.

Confocal images (Figure 5b, Figure S6 and S7b) were obtained by overlaying fluorescence images with bright field images in Image J software.

3. Results and discussion

What are the structural and surface characteristics of GQDs that influence cellular uptake?

3.1. Size, surface functional group and charge characterization

The internalization of two types of GQDs is studied in the present work: NGQDs bottom-up synthesized from a glucosamine precursor and RGQDs synthesized top-down from reduced graphene oxide. Both GQD types are thoroughly characterized to evaluate their physical properties affecting internalization. Transmission Electron Microscopy (TEM) images reveal that NGQDs and RGQDs have size distributions with average diameters of 3.65 ± 1.43 nm and 10.76 ± 6.45 nm respectively (Figure 4c, f). Although there are size differences between NGQDs and RGQDs, both nanomaterials' sizes are below the smallest endocytosis vesicle. Therefore, GQD sizes are not expected to substantially affect their internalization through the endocytosis paths studied, allowing their comparative studies. Both GQDs display graphitic lattices with planar spacings of 0.21 nm for NGQDs and 0.29 nm for RGQDs demonstrated by HRTEM, while their crystallinity is further confirmed by Fast Fourier Transform (FFT) images (Figure 4a, d insets).

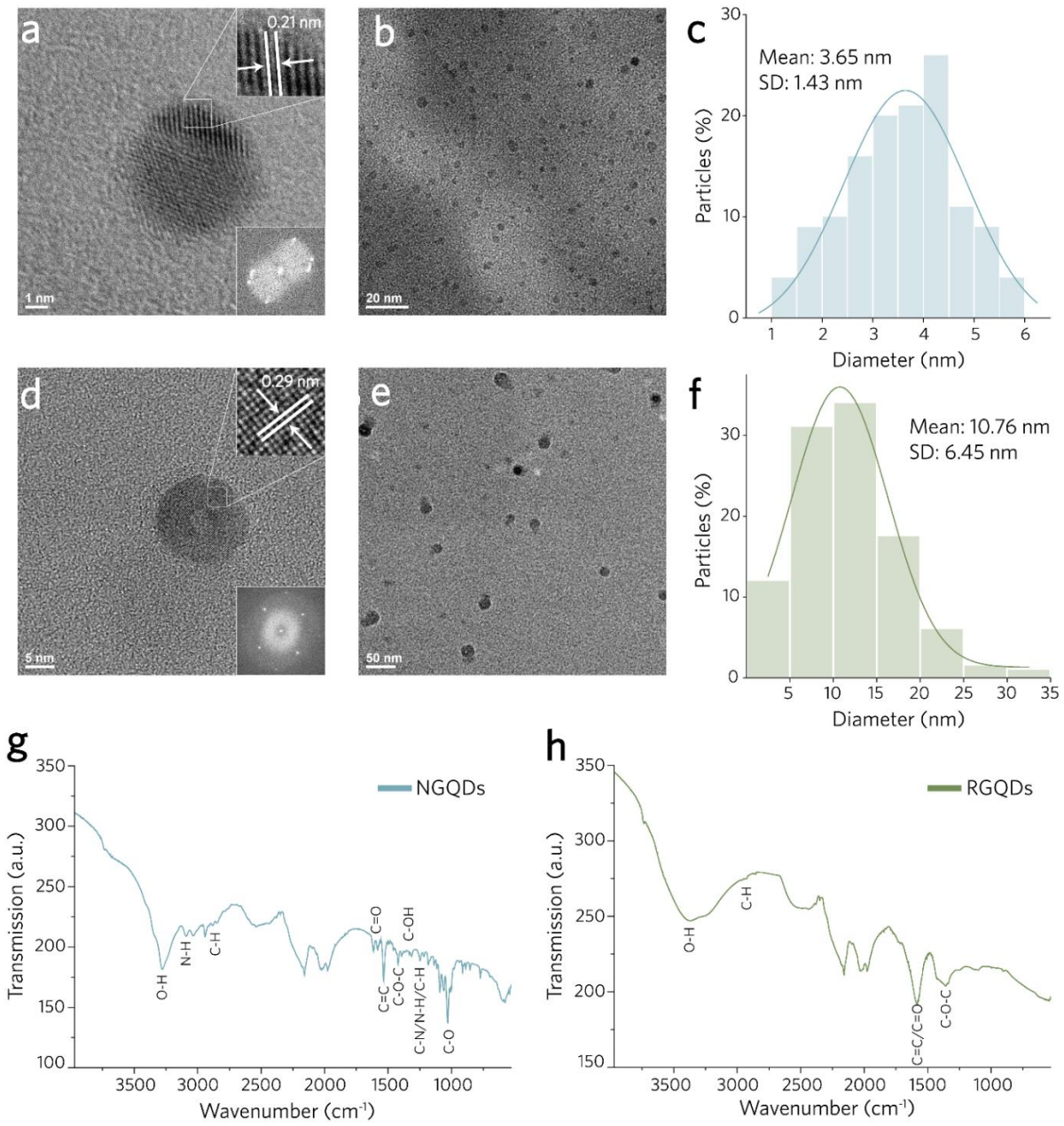

Figure 4. a) HRTEM images of NGQDs, d) RGQDs with insets displaying the interlayer spacings and FFT. b**)** TEM images of NGQDs, e) RGQDs revealing the size distributions. c**)** Nanoparticle size distribution histogram of NGQDs (blue), f) RGQDs (green); the mean and standard deviation of the distributions are indicated within the plots. g) FTIR spectra of NGQDs (blue), h) RGQDs (green); the peaks are marked with the corresponding functional groups present within the structure.

Furthermore, NGQD and RGQD spherical structures and 1-3 and 5-10 nm heights are verified through their AFM height profile analysis (Figure 5). Fourier Transform Infrared Spectra (FTIR) of freeze-dried samples indicate the presence of hydroxyl and carboxyl groups on their surface while NGQDs also exhibit amine group transitions indicative of successful nitrogen doping (Figure 4g, h). Both GQDs possess common bands of O-H,[76] C-H,[77] C=O (of COOH group) and, C-O-C [78] at ~ 3300 cm^{-1}, ~2932 cm^{-1}, 1590 cm^{-1}, and 1400 cm^{-1} respectively. The C=C stretch resides at ~1530 cm^{-1} for NGQDs and at ~1580 cm^{-1} for RGQDs, overlapping with its C=O band (Figure 4g, h) [79]. NGQD FTIR spectra also reveal N-H, C-OH, C-N/N-H/C-H and C-O bands at ~3090 cm^{-1}, ~1330 cm^{-1}, ~1246 cm^{-1}, and ~1028 cm^{-1} (Figure 4g) suggesting the presence of the corresponding functional groups [76].

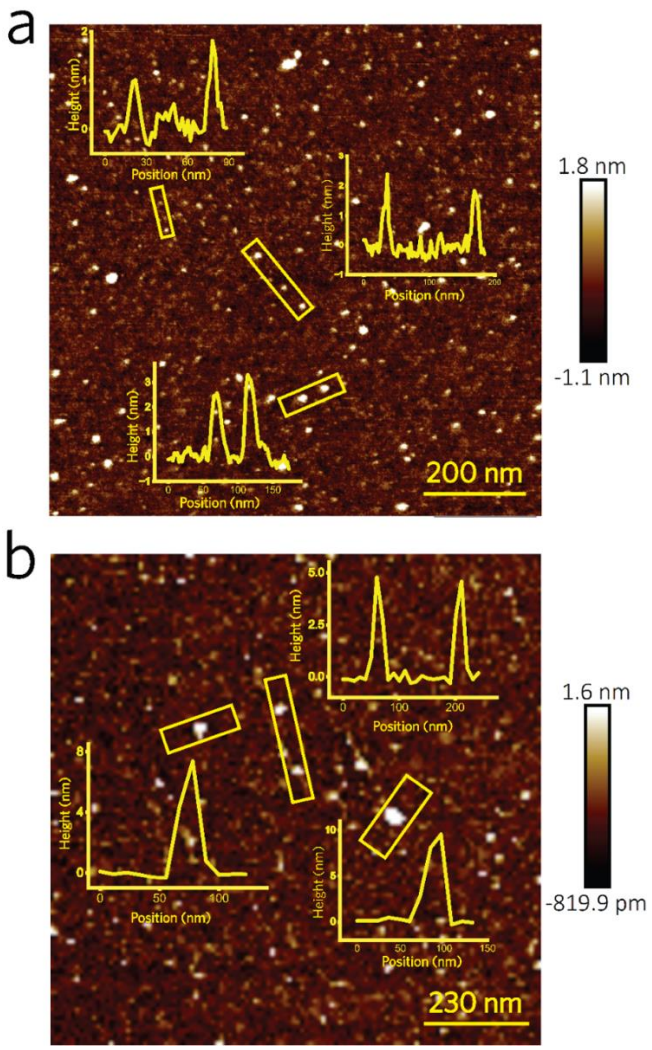

Figure 5. AFM height profiles for a) NGQDs and b) RGQDs.

Moreover, X-Ray Photoelectron Spectroscopy (XPS) studies on NGQDs and RGQDs further confirm the presence of hydroxyl, carboxyl and amine surface functional groups for both nanomaterials (Figure 6 and 7).

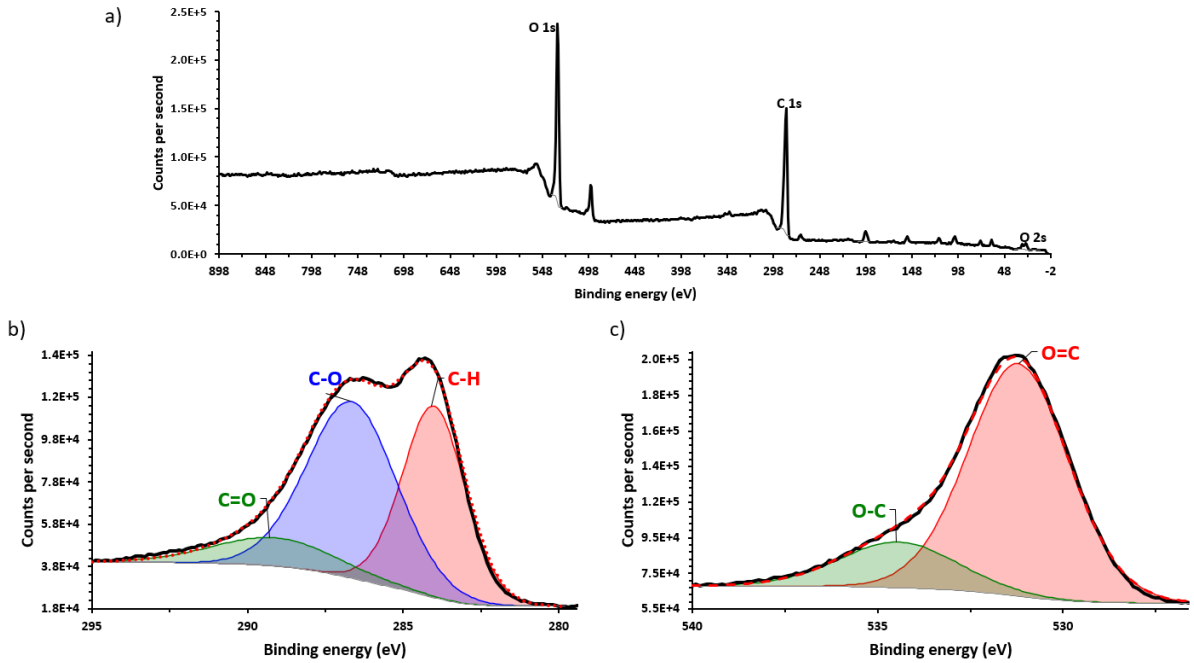

Figure 6. (a) XPS survey spectrum of RGQDs (b) Deconvoluted C1s XPS spectra of RGQDs from Voigt fit with Shirley background correction (c) Deconvoluted O1s XPS spectra of RGQDs from Voigt fit with Shirley background correction.

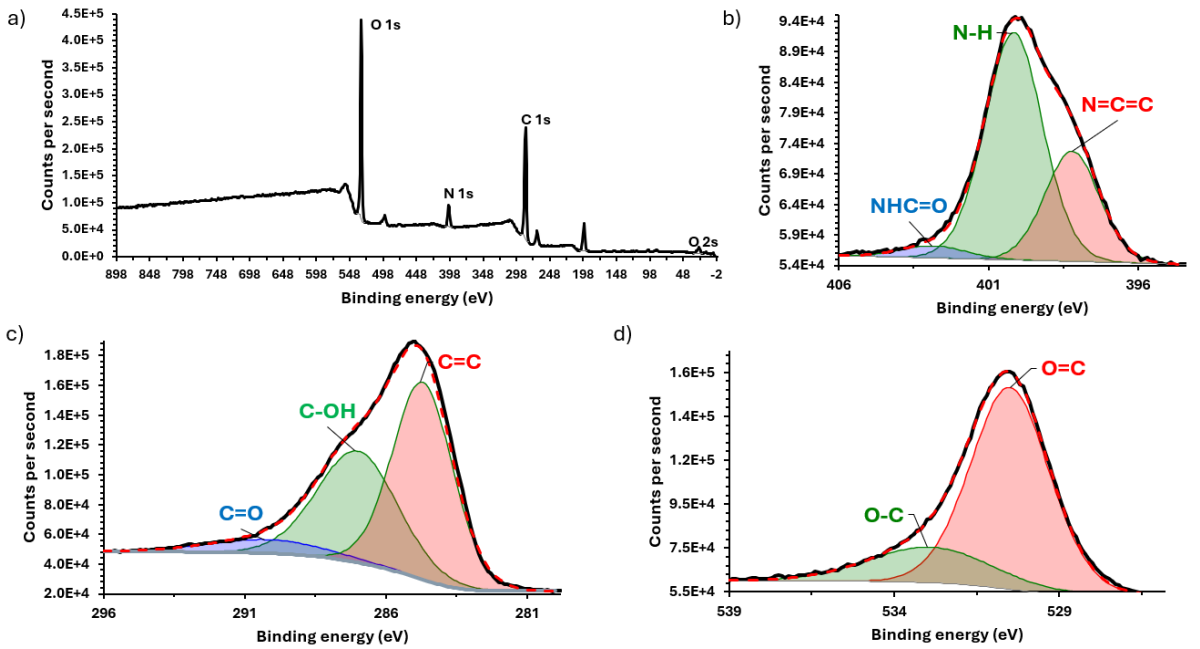

Figure 7. (a) XPS survey spectrum of NGQDs (b) Deconvoluted N1s XPS spectra of RGQDs from Voigt fit with Shirley background correction (c) Deconvoluted C1s XPS spectra of RGQDs from Voigt fit with Shirley background correction (d) Deconvoluted O1s XPS spectra of RGQDs from Voigt fit with Shirley background correction.

The potential of nanoparticle surface charges to initiate specific endocytosis pathways is considered in this work and surface charges of both GQDs are examined via ζ-potential measurements at pH 7 (Figure 8). NGQDs display a positive ζ-potential of +1.8 ± 0.7 mV, likely due to the presence of amine groups, whereas RGQDs show a significantly more negative ζ-potential of -49.4 ± 0.4 mV, attributed to the abundance of hydroxyl and carboxyl groups on their surface.

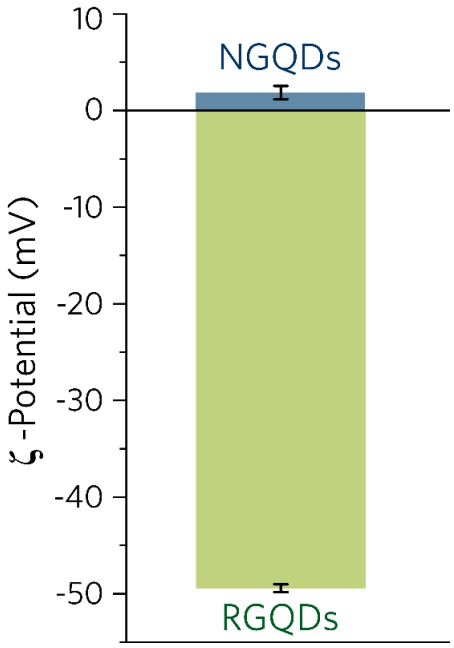

Figure 8. ζ-potentials of NGQDs (blue) and RGQDs (green) at pH 7.

3.2. Optical properties

Endocytosis studies are conducted with the aid of visible fluorescence microscopy; thus, both absorption and fluorescence spectra of both GQD types are analyzed prior to internalization experiments. Both NGQDs and RGQDs exhibit dominant absorption features ~230 nm, attributed to π-π* electronic transitions of C=C (Figure 9a). An absorbance peak at ~278 nm for NGQDs and a shoulder around the same region for RGQDs arise from n-π* transitions of the C=O groups. The characteristic peak ~300 nm in the absorption spectra of NGQDs can be attributed to the π-π* transition of C=N bonds [15]. The abundance of oxygen functional groups, evident from the FTIR and UV-Vis spectra, is responsible for high GQD water solubility (Figure 4g, h and 9a). Both GQD types exhibit broad intrinsic fluorescence in the visible with the peaks at ~500 nm for NGQDs and at ~530 nm for RGQDs with 400 nm

excitation (Figure 9b). This visible emission is attributed to quantum confinement within a plethora of GQD sizes and structures [15].

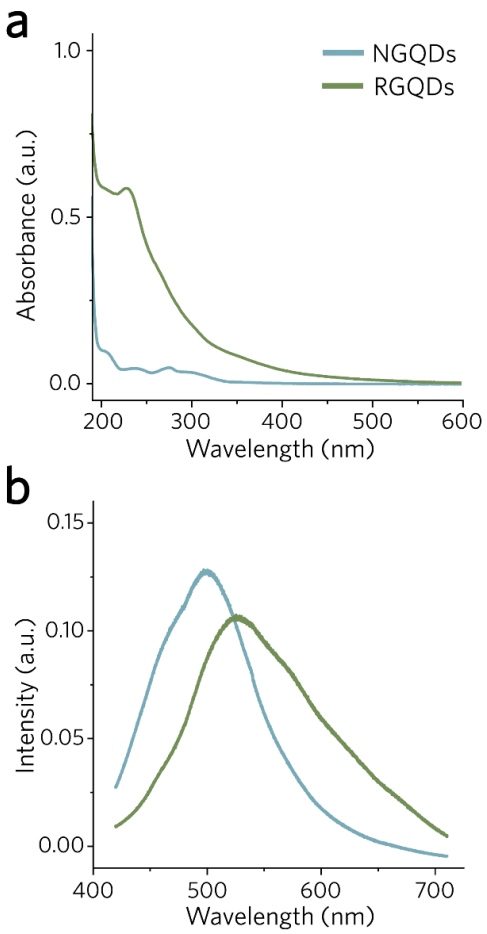

Figure 9. a) Absorbance spectra of NGQDs (blue) and RGQDs (green). b) Visible fluorescence spectra of NGQDs and RGQDs under 400 nm laser excitation.

3.3. Cell Viable concentrations of NGQDs and RGQDs in cancerous and non-cancerous cell lines

MTT assays are further used for the assessment of maximum non-toxic concentration for cell uptake studies in both HeLa and HEK-293 cell lines (Figure 10). Despite the high concentrations used GQDs display remarkable cell viability (>80%), at 0.5 - 1.0 mg/mL in both cell lines. The increase in cell viability above 100% can be explained by the partial degradation of the GQDs in cell environments [5]. Consequently, internalization studies employ biocompatible concentrations of 1.0 mg/mL for NGQDs and 0.5 mg/mL for RGQDs yielding intracellular fluorescence substantial for quantitative analysis of GQD internalization.

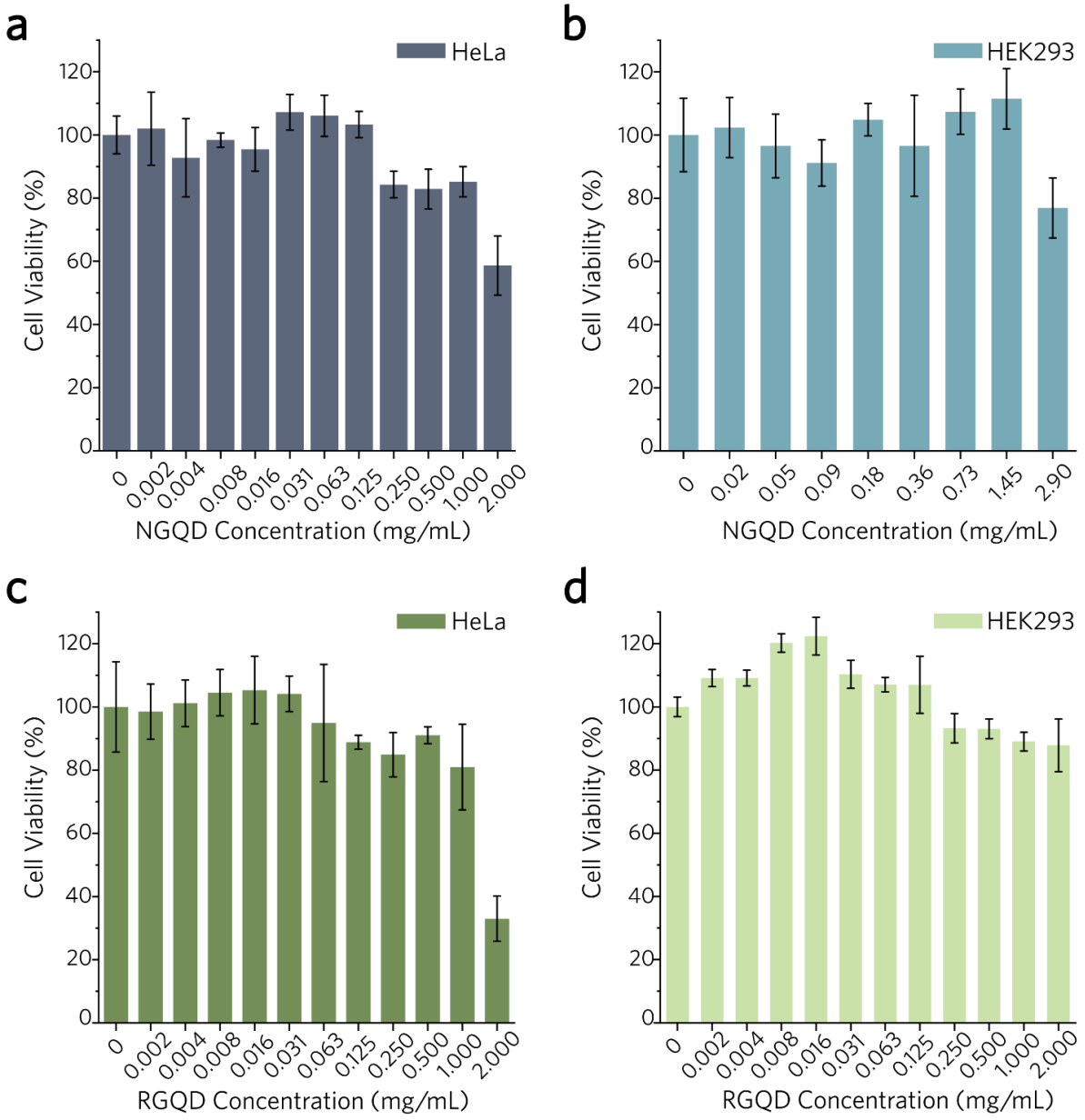

Figure 10. a) Cell viability NGQDs (blue) in HeLa and b) HEK-293 cells. c) Cell viability of RGQDs (green) in HeLa and d) HEK-293 cells as evaluated via MTT assay.

What are the dominant endocytosis pathways for GQD internalization and do these mechanisms differ in cancerous and non-cancerous cell lines?

3.4. Internalization/excretion study of GQDs

In order to consider all the specific effects of six major inhibitors, they are applied separately, while GQD internalization into cancer (HeLa) and non-cancerous (HEK-293) cells possessing different preferential endocytosis pathways is examined. A total of ~100 cells analyzed per inhibitor.

Since all inhibitors were dissolved in DMSO for consistency, instead of a blank control group, cells were treated with DMSO of the same volume to account for its possible effects on cell population. The fluorescence of genistein, filipin, and chlorpromazine inhibitors at the concentrations used in the experiment provides negligible contribution that does not affect fluorescence analysis performed in this work. (Figure 11).

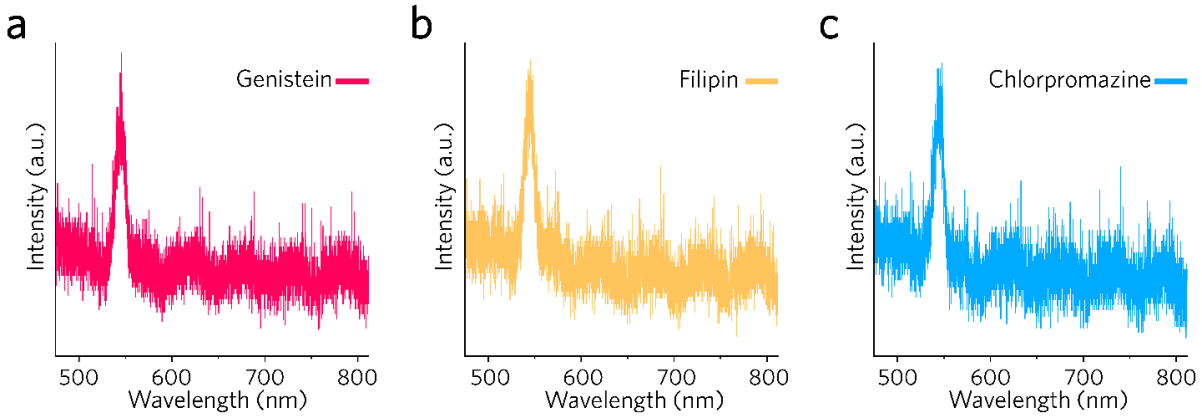

Figure 11. Emission spectra of a) genistein (red), b) filipin (yellow) and c) chlorpromazine (blue) measured at 460 nm excitation at the concentrations used for the experiment. Spectra

displays that these three inhibitors do not contribute to the fluorescence under 460 nm excitation.

The primary internalization study is conducted with the NGQDs, while RGQDs are further used to assess the effects of the charge. This strategy permits a comprehensive analysis, where the effect of each inhibitor is elucidated not merely by its target pathway but through its mechanism of action, detailed in Table 2. Non-internalized GQDs are removed prior to the study by a separate washing step and, thus, do not contribute to observed statistics. Based on TEM size distributions (Figure 4c, f) we expect RGQDs to possess generally greater sizes than NGQDs resulting into somewhat different molarities for different concentrations. However, given that GQDs are a non-stochiometric material with different sizes and structures and simultaneous internalization of several GQDs could potentially occur we are unable to fully predict the molarity effects on endocytosis while we can evaluate the effects of their charge. Internalization is assessed via intracellular GQD fluorescence calculated in the form of corrected total cell fluorescence (CTCF) (Figure 12a). Highest uninhibited NGQD internalization into HeLa cells takes place within the first 6 hours. Due to the relatively low (~20%) CTCF signal observed, a substantial excretion of NGQDs is expected to take place by the 24^{th} hour, complicating the comparative analysis. Conversely, 24 h corresponds to the maximum internalization of NGQDs in HEK-293 cells. The introduction of cytochalasin D adds a pronounced inhibitory effect at the 12-hour mark for NGQDs in both HeLa and HEK-293 cells. Considering the average 3.65 nm sizes of NGQDs (Figure 4c), Macro is unlikely the inhibited pathway. A more plausible explanation posits the disruption of other receptor-

mediated and actin-utilizing pathways, affected by cytochalasin D, such as CME, FEME, Cav, and CLIC/GEEC [61].

In HEK-293 cells, with the introduction of cytochalasin D, an analogous drop in fluorescence is observed at all time points as compared to controls, indicating that FEME, CLIC/GEEC, and, possibly, CME pathways still play a role in NGQD endocytosis (Table 2). A similar pattern of inhibition is observed for genistein at 6 h and 12 h: it drastically inhibits internalization into HeLa cells with substantially smaller impact on HEK-293s. Since genistein inhibits tyrosine kinase, and is shown to inhibit Cav, the lesser inhibition within HEK-293 compared to HeLa may point out that NGQDs prioritize Cav when it is present (Tables 1 and 2). NGQD endocytosis inhibition caused by genistein at the 24^{th} hour time point in HEK-293 cells suggests a potential secondary preference toward FEME in that cell line. Filipin causes a significant decrease in NGQD internalization within HeLa, except for 24 h when the excretion occurs, but only negligible inhibition in HEK-293 cells at all time points. As filipin's mechanism of action, disrupting dynamin by binding to the cholesterol membrane, strongly inhibits FEME and partially - CME, both of these paths are expected to participate in NGQD entry into HeLa cells. At the same time, the absence of such significant inhibition in the HEK-293 cell line suggests that NGQD internalization could utilize lectins as they proceed through CLIC/GEEC pathways in HEK-293 cells, especially given that filipin does not inhibit these pathways and HEK-293 do not possess Cav.

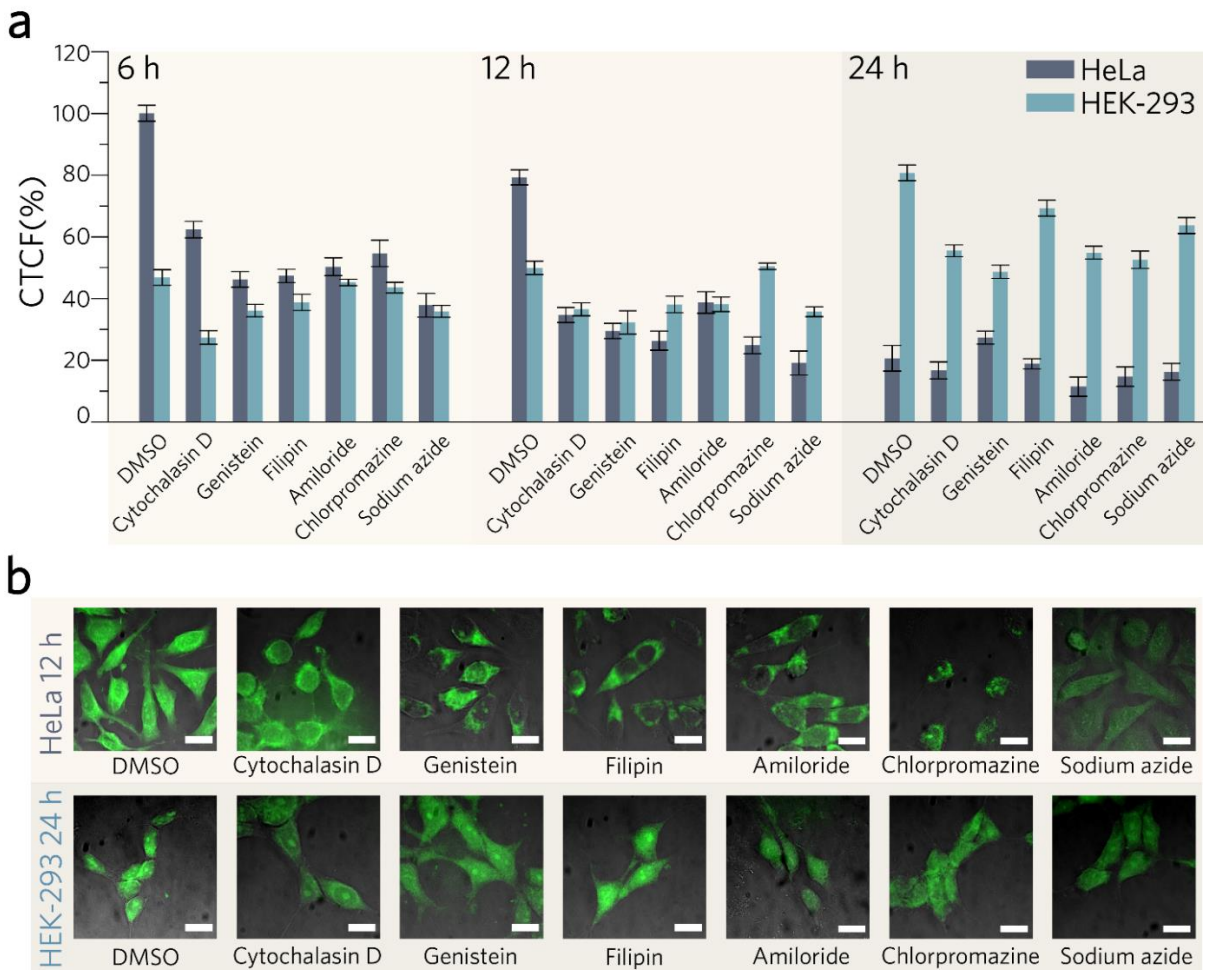

Figure 12. a) Normalized corrected total cell fluorescence (CTCF (%)) of NGQDs in Hela and HEK-293 cells in the presence of chemical inhibitors at 6, 12, and 24 h. b) Bright-field/VIS fluorescence confocal overlay images of HeLa cells treated with NGQDs in the presence of chemical inhibitors at 12 h time point. Scale bar = 10 μm.

Although not as pronounced as in HeLa, amiloride induces considerable inhibition of NGQD entry into HEK-293 cells at 12 and 24 hours. Since, as previously concluded, NGQDs are not expected to enter through Macro due to their size (Figure 4c), the inhibition of their entry by amiloride suggests their internalization through FEME. Amiloride, which induces actin stress fiber disassembly, is expected to cause off-target FEME suppression, indicating

that both cell lines employ FEME for NGQD internalization (Table 2). Furthermore, the observation of a greater comparative NGQD internalization reduction under amiloride inhibition in HeLa versus HEK-293 cells strongly suggests FEME-based NGQD endocytosis in HeLa because amiloride's only off-target pathway is FEME (Table 2). The second strongest inhibition after sodium azide is generated by chlorpromazine at 12-hour time point in HeLa cells. This inhibitor halts the binding of AP2 to clathrin, a key component in CME (Figure 12a), which suggests the important role of CME in GQD internalization. However, it is previously observed that chlorpromazine also acts as an off-target inhibitor for FEME [26, 69]. Thus, the aforementioned significant inhibition cannot be solely attributed to CME, but, rather, CME, FEME and Cav combined (Table 2). Finally, the absence of GQD entry inhibition due to chlorpromazine in HEK-293 at 6 and 12 hours can mistakenly lead to the conclusion that CME and FEME do not play a distinct role in the NGQD internalization process for this cell line. However, a substantial inhibition is observed at the 24^{th} hour time point indicating either an uptake due to combination of FEME and CME or just FEME alone. A very general intermediate conclusion can be drawn from the inhibition pattern provided by sodium azide. Given that it inhibits all energy-dependent pathways, the internalization suppression observed from previous inhibitors and sodium azide conclusively affirms that GQDs internalize through endocytosis. Lesser inhibition caused by sodium azide in HEK-293 cells compared to HeLa cell line, can indicate the importance of passive and/or facilitated diffusion.

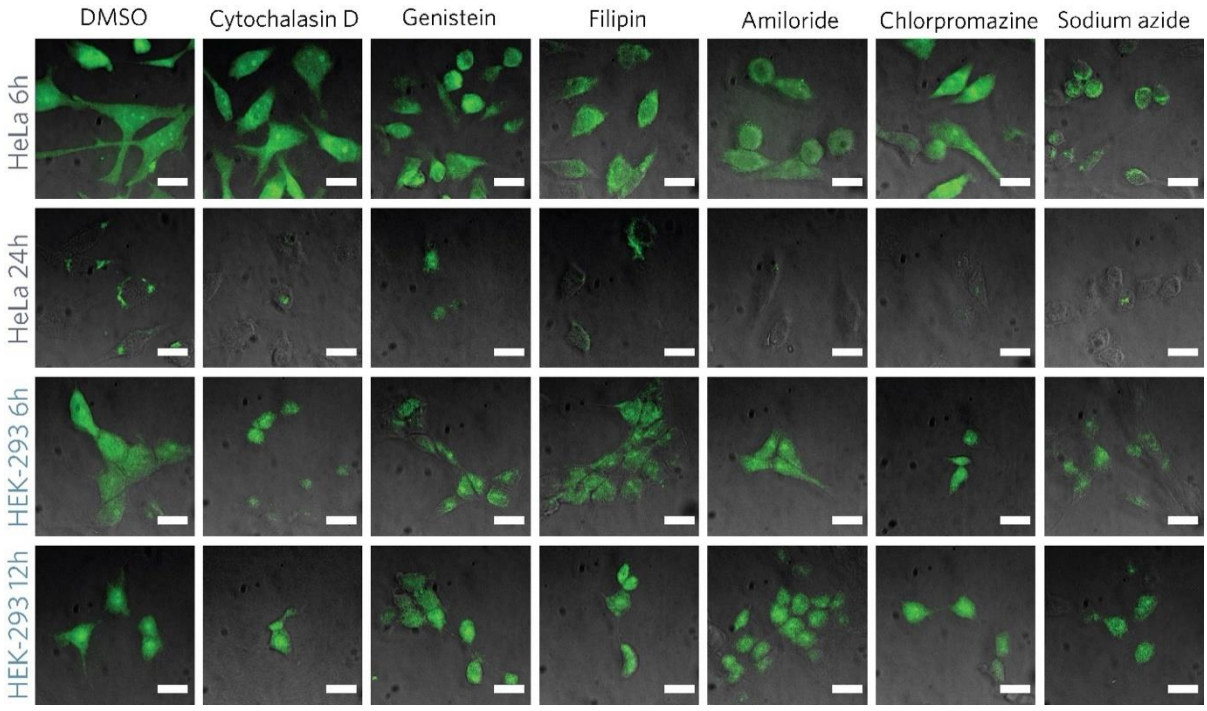

Figure 13. Bright-field/VIS fluorescence confocal overlay images of HeLa cells at 6 and 24h, HEK293 cells at 6 and 12h treated with NGQDs in the presence of chemical inhibitors. Scale bar = 10 μm.

Based on the inhibition effects observed with filipin, amiloride, and chlorpromazine, it is reasonable to infer that NGQDs predominantly enter HeLa cells via FEME and CME. The inhibitory impact of cytochalasin D and genistein further suggests a potential involvement of Cav; however, genistein's lack of specificity precludes a definitive conclusion. For the HEK-293 cell line, a pronounced preference for lectin-dependent CLIC/GEEC endocytosis is evident, supporting negligible inhibition under filipin treatment, which typically inhibits FEME and, to a lesser extent, off-target CME. There is no Cav present in HEK-293 due to a lack of molecular necessary components, and micropinocytosis can’t be considered since its activation requires significantly larger sizes. Chlorpromazine's effect in HeLa cells indicates a marked preference for NGQDs toward CLIC/GEEC endocytosis, as both FEME and CME

appear minimally involved. Thus, one can infer that NGQDs prefer FEME in HeLa cells, closely followed by CME with a lesser inclination towards Cav. In HEK-293 cells, they show a discernible selectivity for CLIC/GEEC endocytosis, with a marginal preference for FEME.

How does surface charge and surface functional groups effect GQD endocytosis?

3.5. RGQD uptake in HeLa cells

Since GQD internalization into HeLa cells predominantly occurs through receptor-mediated endocytosis (mainly CME and FEME), this necessitates a deeper exploration of receptor binding mechanisms to elucidate the reasons for such preference. Since both CME and FEME pathways preferred by the GQDs in HeLa cells use receptors that interact with charged ligands, the effect of the nanomaterial's charge can play a significant role. During the formation of the FEME vesicles, the SH3 domain of endophilin A2 commonly binds to the compatible Guanine nucleotide-binding protein-coupled receptors (GPCRs) such as α_{2a} – and β_1–adrenergic, dopaminergic D3/D4 receptors, muscarinic acetylcholine receptor 4 or the RTKs, such as EGFR, HGFR, VEGFR, PDGFR, NGFR and IGF1R [26]. More than 35% of all FDA-approved drugs act on GPCRs while 70 other FDA-approved drugs act on RTKs [80] outlining the importance of these pathways. One can speculate that GQDs possessing positively-charged amine groups can display an affinity toward such endocytic pathways due to the presence of negative hydroxyl groups on ligand-binding sites of all the GPCRs and RTKs [64, 81]. Conversely, it can be speculated that the positively charged regions on transferrin encompassing Fe^{3+} ions or transferrin receptors used in CME can facilitate a simple

electrostatic attraction of GQDs that display a substantial negative surface charge. This simplistic description offers a speculatory attempt to explain a part of a more complex mechanism (Figure 2b). For instance, a similar charge-dependent uptake for RGQDs can also be facilitated through other pathways such as Ca^{2+}-dependent endocytosis [82].

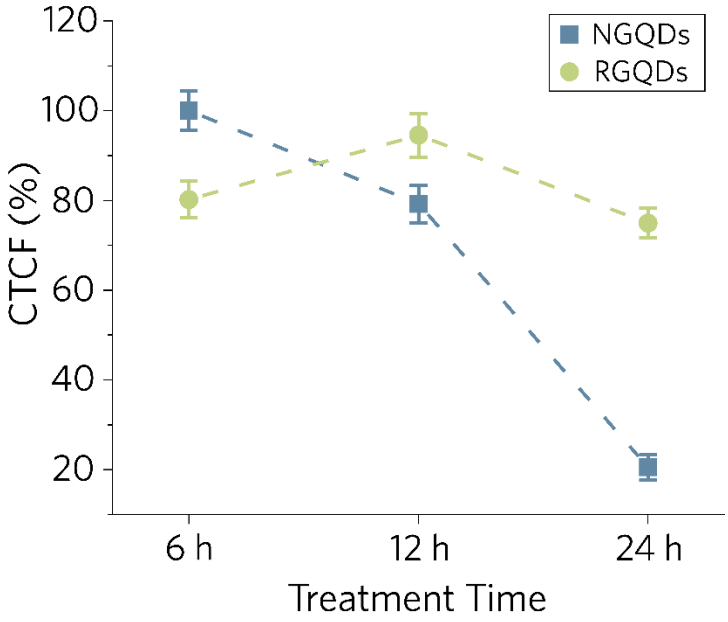

Figure 14. Comparative internalizations of NGQDs and RGQDs in HeLa cells with DMSO treatment (control group) at 6, 12 and 24 h. Corrected total cell fluorescence (CTCF (%)) was normalized to the highest fluorescence value observed (NGQD at 6h) to assess the comparative internalizations of NGQDs and RGQDs when no inhibitors are present.

To experimentally explore charge dependence of GQD endocytosis in HeLa cells, we compare the internalization of negatively charged reduced graphene quantum dots (RGQDs) with a ζ-potential of -49.4 ± 0.4 mV to positively charged NGQDs with a ζ-potential of +1.8 ± 0.8 mV (Figure 8) at 6h, 12h and 24h (Figure 14). This time point is chosen as it yields maximum NGQD internalization and substantial intake of RGQDs.

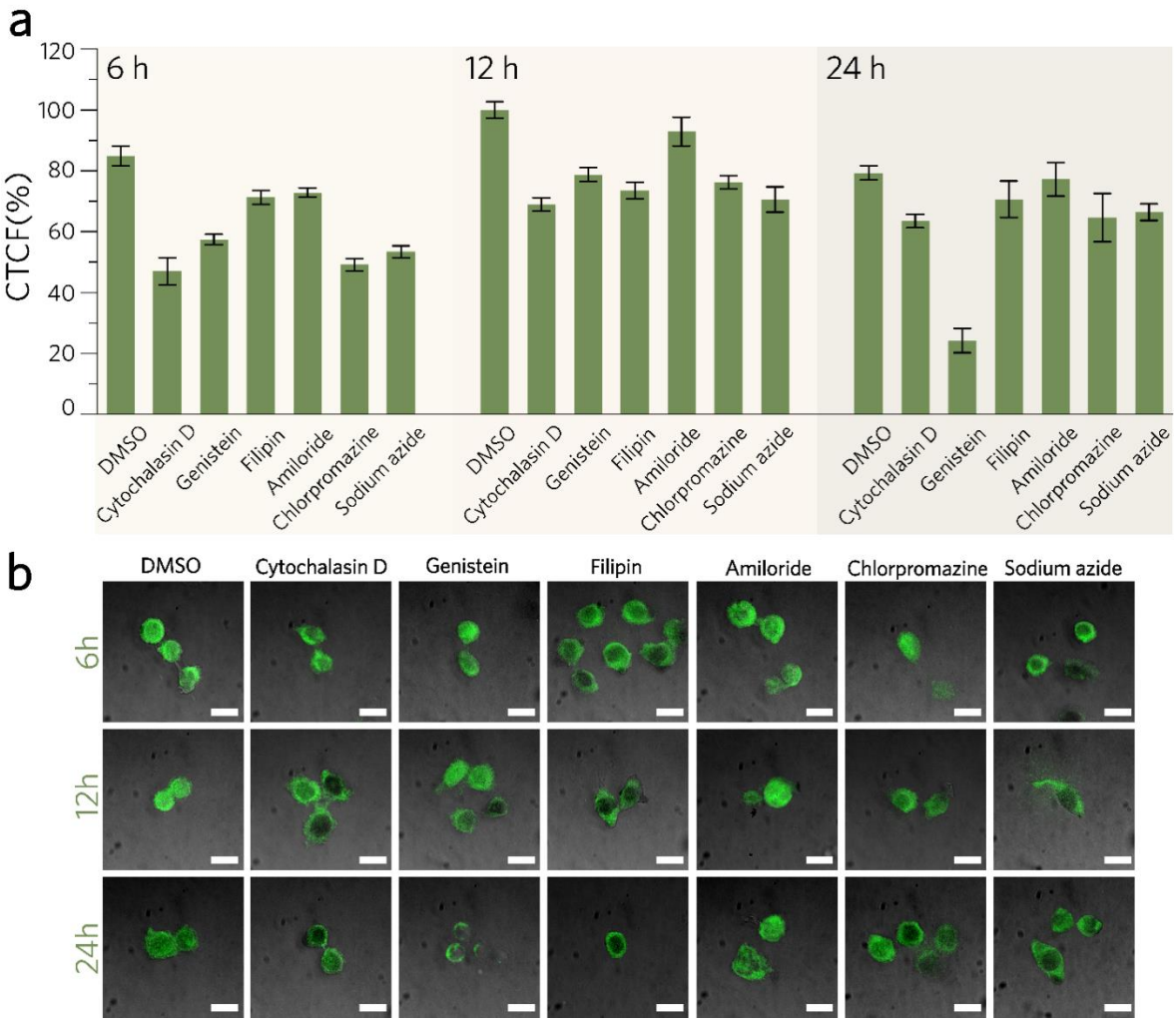

Figure 15. a) Normalized corrected total cell fluorescence (CTCF (%)) of RGQDs in Hela in the presence of chemical inhibitors at 6, 12 and 24 h. b) Bright-field/VIS fluorescence confocal overlay images of HeLa cells treated with RGQDs in the presence of chemical inhibitors at 6, 12 and 24 h. Scale bar = 10 μm.

In this study, NGQDs show ~ 20% more internalization under the control DMSO treatment than RGQDs, while with the introduction of the majority of inhibitors, this ratio varies (Figure 15 and 16). It is noteworthy that both GQDs exhibit similar internalization inhibition patterns compared to their respective control only under cytochalasin D treatment suggesting that actin plays a significant role in the endocytosis of both nanomaterials with no

apparent preference to charge. Genistein's more pronounced inhibitory effect on NGQD internalization, compared to RGQDs, diminishes the likelihood of Cav endocytosis for negatively charged GQDs. The reduced inhibition by filipin and amiloride strongly supports CME as the primary endocytic route for RGQDs, a notion further reinforced by the significant inhibition caused by chlorpromazine. Similar to NGQDs, RGQD internalization is inhibited when cells are treated with the glycolysis inhibitor sodium azide, a general energy-dependent path inhibitor, attesting that RGQD internalization is indeed carried out by endocytosis.

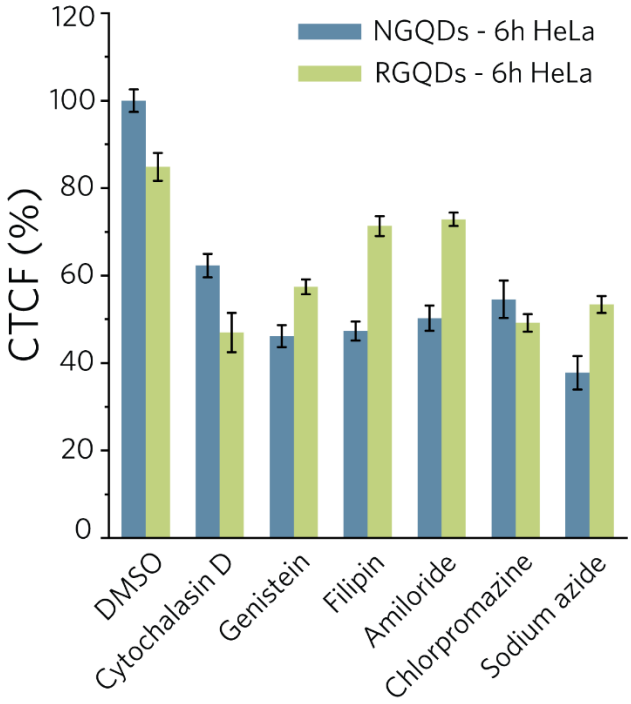

Figure 16. Normalized corrected total cell fluorescence (CTCF (%)) of NGQDs (blue) compared to RGQDs (green) in Hela cells at 6 h.

4. Conclusion

4.1. Conclusion

Endocytosis of graphene quantum dots has been previously studied, yet the specific pathways are still debated, particularly due to insufficient consideration of the biological mechanisms of action and potential off-target effects of inhibitors, resulting in a fragmented understanding and conflicting results in the literature. Our study elucidates the preferential endocytic pathways employed by GQDs in HeLa and HEK-293 cells, achieved through a comprehensive analysis involving six distinct inhibitors, each characterized by unique mechanistic actions. Fluorescence microscopy-derived GQD internalization studies indicate that there is not a single path that GQDs prefer, but rather a combination of certain pathways with an apparent hierarchy in their preferences. An intriguing observation is the reduced internalization of NGQDs in HeLa cells treated with genistein, compared to HEK-293 cells, and suggests a possibility for NGQD internalization via caveolae-mediated pathways in HeLa cells on top of the more significant FEME and CME preference. However, the non-specificity of genistein necessitates a cautious interpretation of these findings. In the HEK-293 cell line, NGQDs primarily use the CLIC/GEEC pathways as their initial choice for endocytosis, suggesting the potential importance of lectin dependence. FEME pathway may carry a secondary preference for NGQDs because of a slight amiloride and significant genistein inhibition observed for NGQD internalization in the HEK-293 cells. Previous studies that are done on GQD derivatives fell short in consideration of the possible non-target inhibition. Therefore, some works resulted in a single conclusion that endocytosis was either carried through Cav and/or CME. Moreover, most of the previous cell uptake pathway studies did not

consider the CLIC/GEEC and FEME as separate pathways while putting them under the clathrin-independent endocytosis umbrella. However, due to the lack of inhibition observed upon the introduction of sodium azide, one cannot rule out the contribution of passive and/or facilitated diffusion of GQDs into the cells when endocytosis pathways are blocked. Finally, considering a variety of pathways in two cell lines allows this study to predict nanomaterial internalization in different cells in which some pathways are more prevalent than others.

Our findings reveal a charge-dependent preference in GQD endocytosis through receptor-mediated pathways. GQD surface chemistry can influence the time spent bound to the cell membrane before internalization. Therefore, successful targeting of receptors that trigger endocytosis can significantly reduce the possibility of provoking cell defense mechanisms such as MPS clearing. Since GQDs in HeLa cells mainly experience receptor-mediated endocytosis (CME, FEME), as opposed to non-receptor-mediated entry (CLIC/GEEC) in HEK-293, it is safe to assume that there is a higher chance of avoiding MPS clearing while using GQDs for cancer treatment applications. NGQDs are inferred to utilize both FEME and CME in HeLa cells, with a predilection for FEME. We propose that NGQD preference to FEME could arise from the attraction of NGQDs' amine groups to the negatively charged functional groups of FEME receptors formed with GPCRs and RTKs (Figure 4b). This preference is further supported by an earlier (6 h) peak internalization observed in HeLa cells that can be explained by FEME's rapid intake mechanism. Supporting FEME internalization is the observation that in the presence of genistein, a tyrosine kinase inhibitor, NGQDs display less internalization compared to RGQDs (Figure 6). Since RTKs are one of the most common receptors that FEME utilizes (Figure 4a), the drop in internalization upon tyrosine kinase inhibition indicates that NGQDs incline towards FEME as their primary choice of cellular uptake in HeLa. Our results

indicate that negatively charged RGQDs predominantly favor CME. Additionally, since HeLa cells used here for RGQD studies do not possess CLIC/GEEC endocytosis vesicles,[55] we are not able to conclude on or rule out the possibility of the lectin-dependent endocytosis for RGQD uptake.[83] CME emerges as the secondary internalization pathway for NGQDs possibly due to the presence of a few negatively charged functional groups on their surface. It is important to point out that the difference in the sizes of NGQDs and RGQDs is not expected to affect any internalization parameters as they both reside within the same endocytosis-relevant size group.

This study challenges the notion of a singular mechanism governing GQD endocytosis, instead proposing a model of preferential pathway usage that varies between cell types and is influenced by the nanomaterial's charge. We previously discussed that both clathrin-independent paths have their specific mechanisms and targeting FEME necessarily can pave the way for nanomaterials' usage in clinical studies since it uses GPCRs and RTKs, which are present in many of the FDA-approved drugs. This nuanced understanding of GQD internalization mechanisms not only deepens our comprehension of GQD-cell interactions but also offers valuable insights for the design of nanomaterials aimed at optimized drug delivery and enhanced efficacy in both *in vivo* and *in vitro* applications.

4.2. Questions answered

i. What are structural and surface characteristics of GQDs that influence cellular uptake?

Two types of graphene quantum dots were studied: nitrogen-doped GQDs (NGQDs) synthesized bottom-up from glucosamine and reduced GQDs (RGQDs) obtained top-down

from reduced graphene oxide. TEM analysis showed average diameters of 3.65 ± 1.43 nm for NGQDs and 10.76 ± 6.45 nm for RGQDs, both below the smallest endocytic vesicle size, indicating that size alone is unlikely to influence pathway selection. HRTEM confirmed graphitic lattice fringes with interlayer spacings of 0.21 nm and 0.29 nm for NGQDs and RGQDs, respectively, while AFM height profiles verified their spherical morphology with heights of 1 - 3 nm and 5 - 10 nm. FTIR spectra revealed hydroxyl and carboxyl groups on both materials, with additional amine group signals in NGQDs confirming successful nitrogen doping. XPS analysis further validated the presence of oxygen- and nitrogen-containing surface functional groups consistent with FTIR results.

Zeta potential measurements indicated a positive charge for NGQDs (+1.8 ± 0.7 mV) due to amine groups and a highly negative charge for RGQDs (−49.4 ± 0.4 mV) arising from hydroxyl and carboxyl groups. Optical analysis showed characteristic π–π* transitions of C=C around 230 nm and n–π* transitions of C=O near 278 nm for both GQDs. Broad intrinsic visible fluorescence was observed at ~500 nm for NGQDs and ~530 nm for RGQDs under 400 nm excitation, confirming their suitability for fluorescence-based internalization studies. MTT assays demonstrated >80% cell viability at 0.5-1.0 mg/mL in both HeLa and HEK-293 cells, validating biocompatible concentrations for subsequent uptake experiments.

These findings establish that both GQD types possess appropriate size, charge, and optical characteristics for endocytoticcellular internalization and fluorescence tracking, with surface charge and functional group composition expected to play key roles in determining uptake behavior.

ii. What are the dominant endocytosis pathways for GQD internalization, and do these mechanisms differ in cancerous and non-cancerous cell lines?

We treated cells with six inhibitors separately and measured NGQD uptake in ~100 cells per inhibitor through corrected total cell fluorescence (CTCF) upon washing to remove non-internalized GQDs. In HeLa, NGQD uptake peaked at 6 h and declined by 24 h, and was strongly reduced by filipin and chlorpromazine at 12 h, indicating major contributions from FEME and CME; inhibition by cytochalasin D and genistein further suggested possible Cav involvement, though genistein's non-specificity limits that conclusion. Amiloride decreased HeLa uptake, consistent with off-target suppression of FEME. In HEK-293, NGQD uptake maximized at 24 h; filipin produced negligible inhibition at all time points. The absence of Cav in this cell line supports a primary preference for lectin-dependent CLIC/GEEC with a secondary FEME contribution. Chlorpromazine effects emerged mainly at 24 h, consistent with late CME and/or FEME involvement. Sodium azide suppressed uptake in both cell lines, confirming energy-dependent endocytosis; its weaker effect in HEK-293 suggests a potential contribution of passive and/or facilitated diffusion. Overall, NGQDs favored primarily FEME and secondarily CME in HeLa and primarily CLIC/GEEC and secondarily FEME in HEK-293. RGQD uptake is delinated within the next question due to their different surface charge.

iii. How do surface charge and surface functional groups influence GQD endocytosis?

To assess the influence of surface chemistry on GQD internalization, we compared positively charged NGQDs ($\zeta = +1.8 \pm 0.8$ mV) and negatively charged RGQDs ($\zeta = -49.4 \pm 0.4$ mV) in HeLa cells at 6, 12, and 24 h. Both materials exhibited similar actin-dependent inhibition under cytochalasin D, indicating that actin polymerization plays a key role in the uptake of both GQD types. However, comparative inhibition patterns revealed distinct charge-dependent preferences in endocytic mechanisms. For instance, genistein more strongly reduced NGQD uptake than RGQD, ruling out the likelihood of caveolin-mediated endocytosis for negatively charged GQDs. Filipin and amiloride produced limited inhibition for RGQDs, whereas chlorpromazine caused a significant reduction in their internalization, confirming clathrin-mediated endocytosis (CME) as the primary route for negatively charged RGQDs. In contrast, NGQDs displayed higher overall uptake (~20% more at 6h) and were most affected by FEME inhibitors, consistent with their positively charged amine groups favoring interactions with negatively charged receptor sites on GPCRs and RTKs. Collectively, these results indicate that **surface charge and functional groups significantly affect pathway selectivity**, with NGQDs preferring receptor-mediated FEME and CME, while RGQDs primarily internalize via CME.

References

1. Mandal, S., *Elucidating carbon dot research coupled with bibliometric analysis.* Next Research, 2024. **1**(2): p. 100051.
2. Chung, S., R.A. Revia, and M. Zhang, *Graphene quantum dots and their applications in bioimaging, biosensing, and therapy.* Advanced Materials, 2021. **33**(22): p. 1904362.
3. Hasan, M.T., et al., *Rare-earth metal ions doped graphene quantum dots for near-ir in vitro/in vivo/ex vivo imaging applications.* Advanced Optical Materials, 2020. **8**(21): p. 2000897.
4. Hasan, M.T., et al., *Near-infrared emitting graphene quantum dots synthesized from reduced graphene oxide for in vitro/in vivo/ex vivo bioimaging applications.* 2D Materials, 2021. **8**(3): p. 035013.
5. Hasan, M.T., et al., *Photo-and electroluminescence from nitrogen-doped and nitrogen–sulfur codoped graphene quantum dots.* Advanced Functional Materials, 2018. **28**(42): p. 1804337.
6. Iannazzo, D., et al., *Graphene quantum dots for cancer targeted drug delivery.* International journal of pharmaceutics, 2017. **518**(1-2): p. 185-192.
7. Ghafary, S.M., et al., *Simultaneous gene delivery and tracking through preparation of photo-luminescent nanoparticles based on graphene quantum dots and chimeric peptides.* Scientific reports, 2017. **7**(1): p. 9552.
8. Valimukhametova, A.R., et al., *Cancer Therapeutic siRNA Delivery and Imaging by Nitrogen-and Neodymium-Doped Graphene Quantum Dots.* ACS Biomaterials Science & Engineering, 2023.
9. Lee, B., et al., *In Vitro Prostate Cancer Treatment via CRISPR-Cas9 Gene Editing Facilitated by Polyethyleneimine-Derived Graphene Quantum Dots.* Advanced Functional Materials, 2023: p. 2305506.
10. Pan, D., et al., *Hydrothermal route for cutting graphene sheets into blue-luminescent graphene quantum dots.* Advanced materials, 2010. **22**(6): p. 734-738.
11. Valimukhametova, A.R., et al., *Five near-infrared-emissive graphene quantum dots for multiplex bioimaging.* 2D Materials, 2024. **11**(2): p. 025009.
12. Doherty, G.J. and H.T. McMahon, *Mechanisms of endocytosis.* Annual review of biochemistry, 2009. **78**: p. 857-902.
13. Tsoi, K.M., et al., *Mechanism of hard-nanomaterial clearance by the liver.* Nature materials, 2016. **15**(11): p. 1212-1221.
14. Topkiran, U.C., et al., *Holistic Investigation of Graphene Quantum Dot Endocytosis.* Small, 2025. **21**(9): p. 2406095.
15. Valimukhametova, A., et al., *Five near-infrared-emissive graphene quantum dots for multiplex bioimaging.* 2D Materials, 2024.
16. Wu, C., et al., *Ultrasensitive detection of protein based on graphene quantum dots with resonance light scattering technique.* Journal of Nanoscience and Nanotechnology, 2018. **18**(4): p. 2680-2685.
17. Li, G., et al., *A ratiometric fluorescent composite nanomaterial for RNA detection based on graphene quantum dots and molecular probes.* Journal of Materials Chemistry B, 2018. **6**(26): p. 4380-4384.

18. Ajgaonkar, R., et al., *Detection of pancreatic cancer miRNA with biocompatible nitrogen-doped graphene quantum dots.* Materials, 2022. **15**(16): p. 5760.
19. Jeong, S., et al., *Graphene quantum dot oxidation governs noncovalent biopolymer adsorption.* Scientific reports, 2020. **10**(1): p. 7074.
20. Gilleron, J., et al., *Image-based analysis of lipid nanoparticle–mediated siRNA delivery, intracellular trafficking and endosomal escape.* Nature biotechnology, 2013. **31**(7): p. 638-646.
21. Rennick, J.J., A.P. Johnston, and R.G. Parton, *Key principles and methods for studying the endocytosis of biological and nanoparticle therapeutics.* Nature nanotechnology, 2021. **16**(3): p. 266-276.
22. Cooper, I., *Transport of small molecules across the blood brain barrier: the prion peptide PrP 106-126 and the neurotransmitter GABA*. 2011, Weizmann Institute of Science.
23. Brown, C.M. and N.O. Petersen, *Free clathrin triskelions are required for the stability of clathrin-associated adaptor protein (AP-2) coated pit nucleation sites.* Biochemistry and cell biology, 1999. **77**(5): p. 439-448.
24. Mu, Q., et al., *Size-dependent cell uptake of protein-coated graphene oxide nanosheets.* ACS applied materials & interfaces, 2012. **4**(4): p. 2259-2266.
25. Ehrlich, M., et al., *Endocytosis by random initiation and stabilization of clathrin-coated pits.* Cell, 2004. **118**(5): p. 591-605.
26. Boucrot, E., et al., *Endophilin marks and controls a clathrin-independent endocytic pathway.* Nature, 2015. **517**(7535): p. 460-465.
27. Howes, M.T., et al., *Clathrin-independent carriers form a high capacity endocytic sorting system at the leading edge of migrating cells.* Journal of Cell Biology, 2010. **190**(4): p. 675-691.
28. Lakshminarayan, R., et al., *Galectin-3 drives glycosphingolipid-dependent biogenesis of clathrin-independent carriers.* Nature cell biology, 2014. **16**(6): p. 592-603.
29. Sathe, M., et al., *Small GTPases and BAR domain proteins regulate branched actin polymerisation for clathrin and dynamin-independent endocytosis.* Nature communications, 2018. **9**(1): p. 1835.
30. Richter, T., et al., *High-resolution 3D quantitative analysis of caveolar ultrastructure and caveola–cytoskeleton interactions.* Traffic, 2008. **9**(6): p. 893-909.
31. Amiel, E., et al., *Pivotal Advance: Toll-like receptor regulation of scavenger receptor-A-mediated phagocytosis.* Journal of Leucocyte Biology, 2009. **85**(4): p. 595-605.
32. Torgersen, M.L., et al., *Internalization of cholera toxin by different endocytic mechanisms.* Journal of cell science, 2001. **114**(20): p. 3737-3747.
33. Damke, H., et al., *Induction of mutant dynamin specifically blocks endocytic coated vesicle formation.* The Journal of cell biology, 1994. **127**(4): p. 915-934.
34. Kurzchalia, T.V. and R.G. Partan, *Membrane microdomains and caveolae.* Current opinion in cell biology, 1999. **11**(4): p. 424-431.
35. Jin, H., et al., *Size-dependent cellular uptake and expulsion of single-walled carbon nanotubes: single particle tracking and a generic uptake model for nanoparticles.* ACS nano, 2009. **3**(1): p. 149-158.
36. Yaron, P.N., et al., *Single wall carbon nanotubes enter cells by endocytosis and not membrane penetration.* Journal of nanobiotechnology, 2011. **9**(1): p. 1-15.

37. Suzuki, N., et al., *Chiral graphene quantum dots.* ACS nano, 2016. **10**(2): p. 1744-1755.
38. Arayachukiat, S., et al., *Bringing macromolecules into cells and evading endosomes by oxidized carbon nanoparticles.* Nano letters, 2015. **15**(5): p. 3370-3376.
39. Luo, N., et al., *Surface-engineered graphene navigate divergent biological outcomes toward macrophages.* ACS applied materials & interfaces, 2015. **7**(9): p. 5239-5247.
40. Lu, Y.-J., et al., *Mechanism of nanoformulated graphene oxide-mediated human neutrophil activation.* ACS Applied Materials & Interfaces, 2020. **12**(36): p. 40141-40152.
41. Tu, Z., et al., *Combination of surface charge and size controls the cellular uptake of functionalized graphene sheets.* Advanced Functional Materials, 2017. **27**(33): p. 1701837.
42. Huang, J., et al., *Mechanism of cellular uptake of graphene oxide studied by surface-enhanced Raman spectroscopy.* Small, 2012. **8**(16): p. 2577-2584.
43. Wang, Q., et al., *Hollow luminescent carbon dots for drug delivery.* Carbon, 2013. **59**: p. 192-199.
44. Shang, W., et al., *The uptake mechanism and biocompatibility of graphene quantum dots with human neural stem cells.* Nanoscale, 2014. **6**(11): p. 5799-5806.
45. Wu, C., et al., *Insight into the cellular internalization and cytotoxicity of graphene quantum dots.* Advanced healthcare materials, 2013. **2**(12): p. 1613-1619.
46. Halder, A., et al., *One-pot green synthesis of biocompatible graphene quantum dots and their cell uptake studies.* ACS Applied Bio Materials, 2018. **1**(2): p. 452-461.
47. Xie, Y., et al., *Graphene quantum dots induce cascadic apoptosis via interaction with proteins associated with anti-oxidation after endocytosis by Trypanosoma brucei.* Frontiers in Immunology, 2022. **13**: p. 1022050.
48. Kumawat, M.K., et al., *Graphene quantum dots for cell proliferation, nucleus imaging, and photoluminescent sensing applications.* Scientific reports, 2017. **7**(1): p. 15858.
49. Manzanares, D. and V. Ceña, *Endocytosis: the nanoparticle and submicron nanocompounds gateway into the cell.* Pharmaceutics, 2020. **12**(4): p. 371.
50. Makvandi, P., et al., *Endocytosis of abiotic nanomaterials and nanobiovectors: Inhibition of membrane trafficking.* Nano Today, 2021. **40**: p. 101279.
51. Xu, L., et al., *Graphene quantum dots in alveolar macrophage: uptake-exocytosis, accumulation in nuclei, nuclear responses and DNA cleavage.* Particle and Fibre Toxicology, 2018. **15**(1): p. 1-17.
52. Xu, L., J. Zhao, and Z. Wang, *Genotoxic response and damage recovery of macrophages to graphene quantum dots.* Science of The Total Environment, 2019. **664**: p. 536-545.
53. Yang, Y., et al., *Endophilin A1 regulates dendritic spine morphogenesis and stability through interaction with p140Cap.* Cell research, 2015. **25**(4): p. 496-516.
54. Torrino, S., et al., *EHD2 is a mechanotransducer connecting caveolae dynamics with gene transcription.* Journal of Cell Biology, 2018. **217**(12): p. 4092-4105.
55. Bitsikas, V., I.R. Corrêa Jr, and B.J. Nichols, *Clathrin-independent pathways do not contribute significantly to endocytic flux.* Elife, 2014. **3**: p. e03970.
56. Thottacherry, J.J., et al., *Mechanochemical feedback control of dynamin independent endocytosis modulates membrane tension in adherent cells.* Nature communications, 2018. **9**(1): p. 4217.

57. Zhang, J., et al., *Distinct functions of endophilin isoforms in synaptic vesicle endocytosis.* Neural Plasticity, 2015. **2015**.
58. Moore, R.H., et al., *Ligand-stimulated β2-adrenergic receptor internalization via the constitutive endocytic pathway into rab5-containing endosomes.* Journal of Cell Science, 1995. **108**(9): p. 2983-2991.
59. Nonnenmacher, M. and T. Weber, *Adeno-associated virus 2 infection requires endocytosis through the CLIC/GEEC pathway.* Cell host & microbe, 2011. **10**(6): p. 563-576.
60. Brenner, S. and E. Korn, *Substoichiometric concentrations of cytochalasin D inhibit actin polymerization. Additional evidence for an F-actin treadmill.* The Journal of biological chemistry, 1979. **254**(20): p. 9982-9985.
61. Fujimoto, L.M., et al., *Actin assembly plays a variable, but not obligatory role in receptor-mediated endocytosis.* Traffic, 2000. **1**(2): p. 161-171.
62. Akiyama, T., et al., *Genistein, a specific inhibitor of tyrosine-specific protein kinases.* Journal of Biological chemistry, 1987. **262**(12): p. 5592-5595.
63. Parton, R.G., B. Joggerst, and K. Simons, *Regulated internalization of caveolae.* The Journal of cell biology, 1994. **127**(5): p. 1199-1215.
64. Goh, L.K. and A. Sorkin, *Endocytosis of receptor tyrosine kinases.* Cold Spring Harbor perspectives in biology, 2013. **5**(5): p. a017459.
65. Araki, N., M.T. Johnson, and J.A. Swanson, *A role for phosphoinositide 3-kinase in the completion of macropinocytosis and phagocytosis by macrophages.* The Journal of cell biology, 1996. **135**(5): p. 1249-1260.
66. Harder, T., et al., *Specific release of membrane-bound annexin II and cortical cytoskeletal elements by sequestration of membrane cholesterol.* Molecular Biology of the Cell, 1997. **8**(3): p. 533-545.
67. Rodal, S.K., et al., *Extraction of cholesterol with methyl-β-cyclodextrin perturbs formation of clathrin-coated endocytic vesicles.* Molecular biology of the cell, 1999. **10**(4): p. 961-974.
68. Kleyman, T.R. and E.J. Cragoe Jr, *Amiloride and its analogs as tools in the study of ion transport.* The Journal of membrane biology, 1988. **105**(1): p. 1-21.
69. Lagana, A., et al., *Regulation of the formation of tumor cell pseudopodia by the Na+/H+ exchanger NHE1.* Journal of cell science, 2000. **113**(20): p. 3649-3662.
70. Wang, L.-H., K.G. Rothberg, and R. Anderson, *Mis-assembly of clathrin lattices on endosomes reveals a regulatory switch for coated pit formation.* The Journal of cell biology, 1993. **123**(5): p. 1107-1117.
71. Torchilin, V.P., et al., *TAT peptide on the surface of liposomes affords their efficient intracellular delivery even at low temperature and in the presence of metabolic inhibitors.* Proceedings of the National Academy of Sciences, 2001. **98**(15): p. 8786-8791.
72. Kim, J.-S., et al., *Cellular uptake of magnetic nanoparticle is mediated through energy-dependent endocytosis in A549 cells.* Journal of veterinary science, 2006. **7**(4): p. 321-326.
73. Vercauteren, D., et al., *The use of inhibitors to study endocytic pathways of gene carriers: optimization and pitfalls.* Molecular Therapy, 2010. **18**(3): p. 561-569.
74. Tsubaki, M. and S. Yoshikawa, *Fourier-transform infrared study of azide binding to the Fea3-CuB binuclear site of bovine heart cytochrome c oxidase: new evidence for a*

redox-linked conformational change at the binuclear site. Biochemistry, 1993. **32**(1): p. 174-182.
75. Ragan, C.I. and E. Racker, *Resolution and Reconstitution of the Mitochondrial Electron Transport System: IV. THE RECONSTITUTION OF ROTENONE-SENSITIVE REDUCED NICOTINAMIDE ADENINE DINUCLEOTIDE-UBIQUINONE REDUCTASE FROM REDUCED NICOTINAMIDE ADENINE DINUCLEOTIDE DEHYDROGENASE AND PHOSPHOLIPIDS.* Journal of Biological Chemistry, 1973. **248**(19): p. 6876-6884.
76. Yang, Q., et al., *Nitrogen-doped carbon quantum dots from biomass via simple one-pot method and exploration of their application.* Applied Surface Science, 2018. **434**: p. 1079-1085.
77. Tang, D., et al., *Graphene oxide derived graphene quantum dots with different photoluminescence properties and peroxidase-like catalytic activity.* RSC advances, 2016. **6**(56): p. 50609-50617.
78. Chhabra, V.A., et al., *Synthesis and spectroscopic studies of functionalized graphene quantum dots with diverse fluorescence characteristics.* RSC advances, 2018. **8**(21): p. 11446-11454.
79. Wang, L., et al., *Gram-scale synthesis of single-crystalline graphene quantum dots with superior optical properties.* Nature communications, 2014. **5**(1): p. 5357.
80. Hauser, A.S., et al., *Trends in GPCR drug discovery: new agents, targets and indications.* Nature reviews Drug discovery, 2017. **16**(12): p. 829-842.
81. Warne, T., et al., *Structure of a β1-adrenergic G-protein-coupled receptor.* Nature, 2008. **454**(7203): p. 486-491.
82. Idone, V., et al., *Repair of injured plasma membrane by rapid Ca2+-dependent endocytosis.* The Journal of cell biology, 2008. **180**(5): p. 905-914.
83. Kramer, R. and E. Canellakis, *The surface glycoproteins of the HeLa cell. Internalization of wheat germ agglutinin-receptors.* Biochimica et Biophysica Acta (BBA)-Biomembranes, 1979. **551**(2): p. 328-348.

VITA

PERSONAL

Ugur Can Topkiran
Mersin, Turkey
January 1, 2000

EDUCATION

Spring 2023-Present

Texas Christian University
Department of Physics & Astronomy
Graduate Student

Fall 2018 - Summer 2022

Izmir Institute of Technology
Department of Physics
Bachelor of Science, Physics

PUBLICATIONS

1. **Topkiran U. C.,** Gasimli A., Durmaz I. L., Paul H., Vashani D., Akkaraju G. R., Naumov A. V. Assessment of in vitro nano-cytotoxicity through fluorescence microscopy via neural network based alive-dead cell classification, Under Review
2. Sharma P., 2Ahluwalia R., Bozkurt I., **Topkiran U. C.,** Dickens A., Valimukhametova A., Agbaglo A., Janesko B., Naumov A. V. Hormone/Neurotransmitter Detection with NIR-Emissive Graphene Quantum Dots Enabled by AI-assisted Spectral Recognition Under Review
3. Valimukhametova A. R., Castro-Lopez N., Sharma P., Malkova K., Gasimli A., **Topkiran U. C.**, Paul H., Vashani D., Zub O., Wormley Jr. F., Naumov A. V. In Vivo and Ex vivo Fluorescence Imaging with NIR-II Emissive Graphene Quantum Dots, *ACS Applied Bio Materials*, Under Review
4. Valimukhametova A. R., Rubina M., Elmanovich I., **Topkiran U. C.,** Vashani D., Paul H., Naumov A. V., Separation of Graphene Quantum Dots by Polarity via Hydrophilic Interaction Liquid Chromatography, *ACS Apllied Nano Materials*, Under Review
5. **Topkiran U. C.**, Valimukhametova A. R., Vashani D., Paul H. , Dorsky A., Sottile O., Johnson D. A., Burnett W., Coffer J., Akkaraju, G. R., Naumov A. V., Holistic Investigation of Graphene Quantum Dot Endocytosis, *Small*, 2025
6. Valimukhametova A. R.,Zub O., Castro-Lopez N., Vashani D., Paul H., **Topkiran U. C.**, Gasimli A., Wormley Jr. F., Naumov A. V., Combination Diagnostics In Vivo: Dual-Mode Ultrasound/NIR fluorescence Imaging with Neodymium- and Thulium-Doped Graphene Quantum Dots, *ACS Applied Bio Materials*, 2025
7. Valimukhametova A. R., Fannon O., **Topkiran U. C.**, Dorsky A., Sottile O., Gonzalez-Rodriguez R., Coffer J., Naumov A. V., Five near-infrared-emissive graphene quantum dots for multiplex bioimaging, *2D Materials*, 2024
8. Lee B., Gries K., Valimukhametova A. R., McKinney R. L., Gonzalez-Rodriguez R., **Topkiran U. C.,** Coffer J., Akkaraju G. R., Naumov A. V., In Vitro Prostate Cancer Treatment via CRISPR-Cas9 Gene Editing Facilitated by Polyethyleneimine-Derived Graphene Quantum Dots, *Advanced Functional Materials*, 2024
9. Valimukhametova A. R., Lee B. H., **Topkiran U. C.**, Gries K., Gonzalez-Rodriguez R., Coffer, J., Akkaraju G. R., Naumov A. V., Cancer Therapeutic siRNA Delivery and Imaging by Nitrogen- and Neodymium-Doped Graphene Quantum Dots, *ACS Biomaterials Science & Engineering*, 2024
10. Yayak Y. O., **Topkiran U. C.**, Yagmurcukardes M., van der Waals Heterostructures of AlAs and InSe: Stacking Dependendent Raman Spectra and Electric Field Dependence of Electronic Properties. *Applied Surface Science*, 2024

11. **Topkiran U. C.**, Yayak Y. O., Sahin H., Yagmurcukardes M., van der Waals Heterostructures of CuI and InSe: Electronic and Vibrational Properties. *Computational Materials Science*, Pre-print
12. Sozen Y., **Topkiran U. C.**, Sahin H. Magnetic Single Layer Nanoribbons of Manganese Oxide: Edge and Width Dependendent Electronic Properties. *Journal of Materials Chemistry C.*, 2022

Abstract

Investigation of Graphene Quantum Dot Endocytosis

By Ugur Can Topkiran, 2025

Department of Physics & Astronomy

Texas Christian University

Thesis Advisor: Anton V. Naumov

Graphene quantum dots (GQDs) have gained popularity in nano-biotechnology due to their multifunctional delivery and imaging capabilities. The outcome of their therapeutic delivery applications relies on understanding cell internalization routes. Current literature presents often conflicting results based on surveying only a few endocytosis inhibitors. Herein, a holistic approach to cell uptake studies by utilizing six different inhibitors while considering their on- and off-target effects on internalization of the GQDs of different charges is provided. Endocytosis paths are explored by tracking intracellular GQD fluorescence in HeLa or HEK-293 cells. Contrary to the previous assumptions of a singular entry route, findings suggest that GQDs enter the cells through several endocytosis paths with some more prevalent than others. Selectivity between the pathways is based on GQD charge and functional groups. Positively charged nitrogen-doped GQDs (NGQDs) predominantly utilize a fast endophilin-mediated endocytosis (FEME) in HeLa cells with a secondary preference for clathrin-mediated endocytosis (CME). In HEK-293 cells NGQDs internalize via clathrin-independent, glycosylphosphatidylinositol-anchored protein-enriched compartments (CLIC/GEEC) and FEME. Conversely, GQDs with a substantial negative surface charge uptake through CME in HeLa cells. The optimization of these mechanisms can enhance GQD applications in biomedicine, ideally streamlining their translation into the clinic.